Measurement of scattering and absorption properties of dust aerosol in a Gobi farmland region of northwest China—a potential anthropogenic influence

Jianrong Bi, Jianping Huang, Jinsen Shi, Zhiyuan Hu, Tian Zhou, Guolong Zhang, Zhongwei Huang, Xin Wang, and Hongchun Jin

Key Laboratory for Semi-Arid Climate Change of the Ministry of Education, College of Atmospheric Sciences, Lanzhou University, Lanzhou 730000, China

Correspondence to: Jianping Huang (hjp@lzu.edu.cn)

Abstract. We conducted a comprehensive field campaign on exploring the optical characteristics of mineral dust in Dunhuang farmland nearby the Gobi deserts of northwest China during spring of 2012. The day-to-day and diurnal variations of dust aerosol showed prominent features throughout the experiment, primarily attributable to frequent dust events and local anthropogenic emissions. The overall average mass concentration of the particulate matter with an aerodynamic diameter less than 10 μm (PM_{10}), light scattering coefficient ($\sigma_{sp,670}$), absorption coefficient ($\sigma_{ap,670}$), and single-scattering albedo (SSA_{670}) were 113$\pm$169 μgm^{-3}, 53.3$\pm$74.8 Mm^{-1}, 3.2$\pm$2.4 Mm^{-1}, and 0.913$\pm$0.05, which were comparable to the background levels in southern United States, but smaller than that in the eastern and other northwestern China. The anthropogenic dust produced by agricultural cultivations (e.g., land planning, plowing, and disking) exerted a significant superimposed effect on high dust concentrations in Dunhuang farmland prior to the growing season (i.e. from 1 April to 10 May). Strong south valley wind and vertical mixing in daytime scavenged the pollution and weak northeast mountain wind and stable inversion layer at night favorably accumulated the air pollutants near the surface. In the afternoon (13:00–18:00 LT, local time), mean SSA_{670} was 0.945$\pm$0.04 that was predominant by dust particles, whereas finer

particles and lower SSA_{670} values (~0.90–0.92) were measured at night, suggesting the potential influence by the mixed dust-pollutants. During a typical biomass burning event on 4 April 2012, $\sigma_{ap,670}$ increased from ~2.0 Mm^{-1} to 4.75 Mm^{-1} and SSA_{670} changed from ~0.90 to ~0.83, implying remarkable modification of aerosol absorptive properties induced by human activities. The findings of this study would help to advance an in-depth understanding of the interaction among dust aerosol, atmospheric chemistry, and climate change in desert source region.

1. Introduction

Asian mineral dust (also known as dust aerosol) in the atmosphere is deemed to exert a profound impact on air quality and climate change. It can perturb the energy budget of the Earth system directly through scattering and absorption of solar and terrestrial radiation (Huang et al., 2009, 2014; Ge et al., 2010; Li et al., 2016) and indirectly by altering cloud microphysical processes and related hydrological cycle (Rosenfeld et al., 2001; J. Huang et al., 2005, 2006, 2010; Yin and Chen, 2007; W. Wang et al., 2010; Creamean et al., 2013; Wu et al., 2016), as well as modifying snow and ice surface albedo (Aoki et al., 2006; Huang et al., 2011; Wang et al., 2013; Qian et al., 2014). In addition, alkaline mineral dust carries abundant organic matters and iron ions deposited on the surface of earth, and hence affects biomass productivity in the North Pacific Ocean and relevant atmosphere-ocean carbon exchange, which plays a pivotal role in the global biogeochemical cycle and carbon cycle (Cao et al., 2005; Jickells et al., 2005; Maher et al., 2010; Shao et al., 2011).

The Taklimakan Desert in northwestern China and Gobi Deserts in southern Mongolia and northern China are widely regarded as two major active centers of dust storms in East Asia (Sun et al., 2001; Zhao et al., 2006; Wang et al., 2008; Ge et al., 2016). These extensive arid and desert zones frequently generate a great deal of tiny soil particles every spring that are uplifted and entrained into the free atmosphere layer via cold frontal cyclones (Zhang et al., 1997; Aoki et al., 2005; Kai et al., 2008; J. Huang et al., 2009, 2010, 2014). Affected by mid-latitude prevailing westerlies,

these dust particles can transport long distances on a subcontinental scale, even sweep across the remote Pacific Ocean and occasionally arrive at the west coast of North America during the peak seasons of strong dust storms (Zhao et al., 2006; Uno et al., 2009, 2011). They then have a far-reaching influence on climatic and environmental changes both regionally and globally. Until now, there have been a large number of intensive field experiments (e.g., ACE–Asia, ADEC, PACDEX, EAST–AIRC) and ground-based aerosol monitoring networks (e.g., AERONET, SKYNET, CARSNET) for probing the Asian mineral dust (Holben et al., 1998; Huebert et al., 2003; Nakajima et al., 2003; Takamura et al., 2004; Eck et al., 2005; Mikami et al., 2006; Huang et al., 2008a; Che et al., 2009, 2015; Li et al., 2011), which is crucial to aid in thoroughly understanding the climatic effects of dust aerosols over East Asian domain. Nevertheless, due to poorly sampled over desert source areas of northwest China, the light scattering and absorption properties of mineral dusts in this region are far inadequate and urgently need to be further surveyed.

The Intergovernmental Panel on Climate Change (IPCC, 2013) reported that the symbol and magnitude of the radiative forcing of mineral dust is greatly reliant on the accurate and reliable knowledge of aerosol total loading, microphysical and chemical characteristics, as well as its spatiotemporal distribution. The current consensus is that nearly pure dust aerosol in the globe has relatively low light-absorption, with single-scattering albedo of ~0.96–0.99 (Dubovik et al., 2002; Anderson et al., 2003; Uchiyama et al., 2005; Bi et al., 2014, 2016), which depends principally on the fraction and mixing ways of ferric iron oxides (i.e. hematite and goethite) in dust (Sokolik and Toon, 1999; Lafon et al., 2004, 2006). However, the coexistences of both mineral dust and other types of aerosols originated from diverse human activities (e.g., coal combustion, mobile source emissions, and biomass burning) are ubiquitous in the real atmosphere, which increases the complexity and variability to aerosol key parameters (Arimoto et al., 2004; Xu et al., 2004; Wang et al., 2015). When the lofted dust plumes in desert source areas are traveled eastward across the polluted regions, they commonly mix with anthropogenic pollutants and enhance heterogeneous chemical reactions with other reactive gas species, and then may remarkably alter

88 their chemical and microphysical properties (Arimoto et al., 2006; Li and Shao et al.,

89 2009; Nie et al., 2014). It is well documented that the mineral dust might have already

90 mixed with polluted aerosols in near dust source regions of northwest China (i.e.

91 Inner Mongolian Gobi desert), besides the mixing processes on the transport pathway

92 (K. Huang et al., 2010). Xu et al. (2004) indicated that both dust aerosol and local

93 pollution sources coexisted in Yulin nearby the Mu Us desert of northwest China

94 during April 2001, which produced a significant influence on aerosol properties in the

95 region. Likewise, Li et al. (2010) analyzed trace gases and aerosols observed at

96 Zhangye (39.082°N, 100.276° E, 1460 m above MSL), a rural site within the Hexi

97 Corridor in northwest China during spring 2008, and uncovered that the mixing

98 between mineral dust and anthropogenic air pollutants can be omnipresent in this area,

99 including at nighttime or during severe dust events. It implies that prior to moving out

100 from the source region, dust particles were likely in connection with pollutants. For

101 the sparsely populated and lesser anthropogenic affected desert source regions in

102 northwest China (e.g., the Taklimakan Desert and its adjacent areas), the interaction

103 between local pollutions and mineral dust is deserved to explore in depth. This is of

104 prime importance to ascertain the relative contributions of two different aerosol

105 sources in atmospheric chemistry and regional climate change.

106   To advance a better understanding of the drought processes and dust-relevant

107 climatic impacts in northwest China (Huang et al., 2008b; Bi et al., 2011; G. Wang et

108 al., 2010), the Semi-Arid Climate and Environment Observatory of Lanzhou

109 University (henceforth referred to as SACOL, http://climate.lzu.edu.cn/english/)

110 carried out a comprehensive field campaign in Dunhuang during spring of 2012.

111 Dunhuang is situated at the westernmost fringe of Hexi Corridor in Gansu province,

112 close to the eastern edge of Kumtag Desert and about 450 km in the downwind zone

113 of Taklimakan Desert. It is an important town of the ancient Silk Road and the

114 transportation junction to the ancient western region, central Asia and Europe, which

115 has become a world-famous tourist city with a residential population of 200,000. The

116 agriculture and tourism are the dominant economic industries in Dunhuang. An array

117 of ground-based remote sensing and in situ instruments were set up during the

118 intensive period, which sought to investigate the aerosol key properties and its
119 climatic effect on regional scale (Bi et al., 2014). This study especially aims at
120 exploring the light scattering and absorption characteristics of mineral dust and
121 elucidates a potential anthropogenic influence. In the following, we first introduce the
122 site information and integrated measurements in Section 2. The primary results and
123 discussion are described in Sect. 3. The concluding remarks are given in Sect. 4 and
124 followed by the data availability in Sect. 5.

2. Site and instrumentation

2.1. Site information

127 SACOL's Mobile Facility (SMF) was deployed at Dunhuang farmland (40.492° N,
128 94.955° E, 1061 m above MSL) from 1 April to 12 June 2012. The site is a tiny
129 isolated oasis encompassed by east-west oriented Gobi desert and arid zones in
130 northwest China, with the Mingsha Shan (Echoing-Sand Mountain, elevation: ~1650
131 m) and Sanwei Mountain (elevation: ~1360 m) to the southwest, and the Beishan
132 Mountain (elevation: ~2580 m) to the north (Ma et al., 2013). The underlying surface
133 is typically covered with Gobi desert and saline-alkali land, and the principal
134 vegetation types consist of extremely sparse Alhagi. Dunhuang farmland is an
135 important agricultural base in Gobi desert, mainly planting hami melon and cotton.
136 There are not any significant manmade pollution sources (e.g., large-scale industries
137 or coal-fired power plants) around the monitoring station. The southwest-northeast
138 oriented National Highway 215 is about 400 m away from the west of the site (Figure
139 1a). The nearest Xihu township (with total population of 13,800) is approximately 7
140 km to the north of Dunhuang farmland, along with some scattered villages stretching
141 from west to east. Meanwhile, the station is located in the northeast of Dunhuang city
142 (~45 km), at the west of Guazhou country (~70 km), and at the southwest of Liuyuan
143 town (~80 km). In general, the major anthropogenic emission sources at Dunhuang
144 farmland likely include coal combustion from domestic heating and cooking, mobile
145 sources emissions from vehicle exhaust gas, and biomass burning from crop residue
146 and traditional ritual activities, which are ordinarily considered to be a puny

147 contribution to the mineral dust in present-day climate models. The climate pattern

148 here is characterized as extreme drought but with a moderate temperature during the

149 whole sampling period (temperature: 18.3±8.1℃, relative humidity, RH: 21.9±16.5%,

150 mean ± standard deviation). Thereby the dust storms frequently take place in this

151 region from spring to early summer. Figure 1(b) shows the overall mean UV aerosol

152 index (AI) from 1 April to 12 June 2012 obtained from the Ozone Monitoring

153 Instrument (OMI) absorbing aerosol products (Torres et al., 2007). The AI dataset is a

154 very good indicator for mapping the distribution of absorbing aerosols (mainly black

155 carbon and dust). The distributions of high AI values (>0.7) are well consistent with

156 the dust-dominated geomorphological features in arid and semiarid regions (i.e.

157 Taklimakan Desert and Gobi deserts). It is very obvious that Dunhuang (marked with

158 a pentagram) is also situated at the primary dust belt of northwest China, as presented

159 in Figure 1b.

160 **2.2. Aerosol measurements**

161 An aerosol integrated observing system is installed in the laboratory of SMF and

162 utilized to continuously measure aerosol optical properties and size distribution in the

163 field. Prior to the experiment, the in-situ aerosol instruments and broadband

164 radiometers were newly purchased and calibrated by the manufacturers (Bi et al.,

165 2014). Table 1 summarizes the basic specification, measured variables, and accuracy

166 of surface-based instruments deployed at Dunhuang farmland throughout the

167 experiment. We shall describe sequentially as below.

168 An ambient particulate monitor (Model RP1400a, Rupprecht and Patashnick

169 Corp.) can collect the in situ mass concentration of the particulate matter with an

170 aerodynamic diameter less than 10 μm (PM_{10}) based on Tapered Element Oscillating

171 Microbalance (TEOM) technique. The measurement range and accuracy of PM_{10}

172 concentration levels are normally 0–5 gm^{-3} and 0.1 μgm^{-3}, respectively. The heating

173 temperature (~50℃) of the sampling tube may cause a partial loss of volatile and

174 semivolatile aerosol compounds and hence bring about a negative signal. In this study,

175 we eliminate all the negative values of PM_{10} concentrations, which account for less

176 than 1% of total data points.

177   An integrating nephelometer (Model 3563, TSI Inc.) is designed to simultaneously

178 measure the total scattering coefficients (σ_{sp}) and hemispheric backscattering

179 coefficients (σ_{bsp}) of aerosol particles at three wavelengths of 450, 550, and 700 nm,

180 with the σ_{sp} detection limits of 0.44, 0.17, and 0.26 Mm^{-1} (1 Mm^{-1}=10^{-6} m^{-1}),

181 respectively (signal-to-noise ratio of 2) (Anderson et al., 1996). To quantify the

182 instrument drift and improve accuracy, we periodically perform the routine calibration

183 using air and high-purity CO_2 gases. Furthermore, the truncation errors of

184 near-forward scattering (i.e. nonideal angular effects) are corrected according to the

185 method of Anderson and Ogren (1998). The observed ambient RH values are mostly

186 smaller than 40% throughout the entire period. It is well-documented that RH-induced

187 the variations in aerosol light scattering coefficients are minimized under a low

188 sampling stream RH of 10–40% (Covert et al., 1972). In this paper, we computed the

189 scattering Ångström exponent at 450–700 nm (SAE 450/700 nm) from σ_{sp} at 450 nm

190 and σ_{sp} at 700 nm by utilizing a log-linear fitting algorithm. And thus σ_{sp} at 670 nm

191 ($\sigma_{sp,670}$) was logarithmic interpolated between $\sigma_{sp,\,450}$ and $\sigma_{sp,\,700}$.

192   A multi-angle absorption photometer (MAAP Model 5012, Thermo Electron

193 Corp.) is capable of observing the aerosol light absorption coefficient at 670 nm

194 ($\sigma_{ap,670}$) by filter based methods without requirement of post-measurement data

195 correction or parallel-measured aerosol light-scattering coefficients (Petzold et al.,

196 2002). The instrument detects an emitted light at 670 nm in the forward and back

197 hemisphere of airborne aerosols deposited on a fiber filter, which is used to improve

198 multiple scattering effects in the aerosol optical properties via a radiative transfer

199 scheme (Petzold et al., 2002, 2005). The sample flow rate is 1000 L/h, with flow error

200 of < 1%. We made use of a specific absorption efficiency at 670 nm of 6.5±0.5 m^{2}g^{-1}

201 to estimate black carbon (BC) concentration from $\sigma_{ap,670}$ as recommended by Petzold

202 et al. (2002).

203   An Aerodynamic Particle Sizer (APS) spectrometer (Model 3321, TSI Inc.) can

204 continuously provide the real-time, high-resolution aerosol size distribution with

205 aerodynamic diameters from 0.5 to 20 μm range (52 channels). When extreme dust

206 episodes outbreak, an aerosol diluter (Model 3302A, TSI Inc.) is operated in series

207 with APS to reduce particle concentrations in high-concentration aerosols, which

208 offers a representative sampling that meets the input requirements of the APS

209 spectrometer. All the mentioned-above aerosol datasets were acquired at 5-minute and

210 hourly averages, and reported for sampling volumes under standard air conditions (i.e.,

211 1013.25 hPa and 20 ℃).

2.3. Other ground-based measurements

213 A Micro-Pulse Lidar (Model MPL–4, Sigma Space Corp., U.S.A.) is a compact

214 and unattended apparatus for providing continuous data information of extinction

215 coefficient and depolarization ratio profiles of aerosols and clouds (Welton et al.,

216 2000). The MPL–4 emits a laser beam at 527 nm wavelength from a Nd:YLF pulsed

217 laser diode and receives the attenuated backscattering intensity and depolarized

218 signals from aerosol particles or cloud droplets with a 30-meter vertical resolution and

219 a 1-minute average interval. And we can acquire the accurate backscattering profile

220 by means of a series of corrections (e.g., dead time, background signal, afterpulse,

221 overlap, and range-corrected) according to the standard methods (Campbell et al.,

222 2002). The detailed data acquisition and retrieval algorithms of the lidar system can

223 be referred to the publications of Campbell et al. (2002) and Z. Huang et al. (2010).

224 A weather transmitter (Model WXT–520, Vaisala, Finland) is set up on the top of

225 the SMF trailer and recorded the air temperature (T in ℃), relative humidity (RH),

226 ambient pressure (P, unit: hPa), wind speed and wind direction at 10 seconds interval.

227 In this article, we calculated the 5-minute and hourly averages from the raw data.

228 A dozen of state-of-the-art broadband radiometers were installed in a row on a

229 standard horizontal platform (~4 m above the surface) where the field of view was

230 unobstructed in all directions (Bi et al., 2014). The direct normal irradiance and

231 diffuse irradiance were independently measured by an incident pyrheliometer (Model

232 NIP, Eppley Lab.) and by a ventilated and shaded pyranometer (Model PSP, Eppley

233 Lab.), which were mounted on a two-axis automatic sun tracker (Model 2AP,

234 Kipp&Zonen). The global irradiance (0.285–2.8 μm) and downward longwave

235 irradiance (3.5–50 μm) were respectively gathered from a ventilated PSP pyranometer

236 and a ventilated and shaded pyrgeometer (Model PIR, Eppley Lab.). All irradiance

quantities were stored in a Campbell data logger with 1-minute resolution. Additionally, a Total Sky Imager (Model TSI–880, YES Inc.) provides high-resolution sky pictures every one minute during the daytime, which can detect and identify the important weather conditions, such as dust storm, smoky pollution, rainy day, cloudy or cloudless days.

2.4. MERRA reanalysis products

The MERRA (Modern–Era Retrospective Analysis for Research and Applications) reanalysis assimilates a variety of conventional observations (i.e. temperature, pressure, height, wind components) from surface weather stations, balloons, aircraft, ships, buoys, and satellites from 1980 to the present, which is primarily committed to improve upon the hydrologic cycle and energy budget for the science community (Rienecker et al., 2011). In this paper, we took advantage of the 6-hourly average wind fields at 500 hPa and 850 hPa levels from the MERRA reanalysis products.

3. Results and discussion

3.1 Aerosol optical properties

The aerosol single-scattering albedo (SSA) at 670 nm is defined as the ratio of the light scattering coefficient ($\sigma_{sp,670}$) to the total extinction coefficient (the sum of $\sigma_{sp,670}$ and $\sigma_{ap,670}$). The SSA reflects the absorptive ability of aerosol particle and is a key quantity in determining the sign (warming or cooling) of aerosol radiative forcing for a certain underlying surface (Hansen et al., 1997; Ramanathan et al., 2001).

Figure 2 delineates the time series of hourly average PM_{10} mass concentration, aerosol optical properties and size distribution at Dunhuang farmland during the whole period. The overall mean, standard deviation, median, and different percentiles of aerosol optical properties are also tabulated in Table 2. Aerosol optical features exhibit dramatic day-to-day variations at Dunhuang. It is apparent that aerosol loadings in April and early May are systematically higher than that in late May and June, which agrees well with the results of columnar aerosol optical depths derived from sky radiometer (Bi et al., 2014). This is chiefly attributed to the invading mineral particulates from the frequent occurrences of intense dust storms in spring season.

The highly unstable synoptic cyclones (i.e. Mongolian cyclone) are regularly hovering about the northern China and Mongolia in springtime, which trigger high-frequency strong surface winds (Sun et al., 2001; Shao et al., 2011). The rising temperature in this season leads to the melting of frozen soil and snow cover, leaving behind a loose land surface and abundant bare soil sources, therefore affords a favorable condition for dust storms. In addition, the contributions of local dust emissions couldn't be ignored. We have clearly recorded that there were numerous agricultural cultivated operations (e.g., land planning, plowing, and disking) throughout the Dunhuang farmland district from 1 April to 10 May, which produced a great amount of agricultural soil particles under strong winds, and thus had a significant superimposed effect on elevated dust loading in the source and downwind regions prior to the growing season. Figure S1 also presents visual photos of a variety of agricultural cultivations in Dunhuang farmland before the planting period, which supplies direct and powerful evidences for supporting our results. Those dust aerosols originated from disturbed soils induced by human activities are interpreted as anthropogenic dust (Tegen and Fung, 1995). Recently, some investigators estimated that anthropogenic dust could account for approximately 25% of the global dust load (Ginoux et al., 2012; Huang et al., 2015), and more than 53% of the anthropogenic sources mostly came from semi-arid and semi-wet zones (Huang et al., 2015; Guan et al., 2016). Nonetheless, it still remains a challenging task to distinguish between the natural and anthropogenic fractions of mineral dust by employing a onefold technology, for instance, laboratory analysis, in situ measurements, model simulations, active and passive remote sensing methods (e.g., multichannel lidar, sun/sky radiometer), which should be combined together (Bi et al., 2016). The overall mean PM_{10} concentration was 113 ± 169 μgm^{-3} (mean ± standard deviation), which is ~39% lower than the 184.1 ± 212 μgm^{-3} average level in Dunhuang (40.1° N, 94.6° E, 1139 m) during the spring of 2004 (Yan, 2007), and ~26% smaller than the value of 153 ± 230 μgm^{-3} measured at Zhangye (39.082° N, 100.276° E, 1460 m) during spring of 2008 (Li et al., 2010). Wang et al. (2015) obtained a total average PM_{10} concentration of 172 ± 180 μgm^{-3} at SACOL during late spring of 2007 (from 25 April to 25 June). And the mean

296   PM_{10} levels at Hunshan Dake sandland in northern China during spring of 2001

297   varied between 226 and 522 μgm^{-3} (Cheng et al., 2005).

298   The hourly average aerosol light scattering coefficient at 670 nm ($\sigma_{sp,670}$) was

299   53.3±74.8 Mm^{-1}. The big standard deviations of PM_{10} and σ_{sp} are possibly associated

300   with the injection of dust particles during the intense dust storms. Our result was

301   about a factor of 3 lower than the σ_{sp} at 500 nm in mentioned-above other sites over

302   northern China (i.e., 126±90 Mm^{-1} for Dunhuang, 159±191 Mm^{-1} for Zhangye,

303   164±89 Mm^{-1} for SACOL). Despite relatively small magnitude, the aerosol light

304   absorption coefficient at 670 nm ($\sigma_{ap,670}$) also presented pronounced variations, with

305   an average value and a maximum of 3.2±2.4 Mm^{-1} and 25.0 Mm^{-1}, respectively. This

306   result was a factor of 2 smaller than Yulin (6±11 Mm^{-1}) nearby Mu Us desert in

307   northwest China (Xu et al., 2004), and a factor of 5~7 far less than that at Shangdianzi

308   rural site (17.5±13.4 Mm^{-1}) in northern China (Yan et al., 2008) and Lin'an site (~23

309   Mm^{-1}) in southern China (Xu et al., 2002). The mean light scattering and absorption

310   coefficients in this study are comparable to the background levels (~46.9±16.9 and

311   2.5±1.1 Mm^{-1}) in Southern Great Plain of U.S.A (Delene and Ogren, 2002). This

312   suggests that extremely low levels of light absorption and scattering substances are

313   widely distributed throughout the Dunhuang region during the spring of 2012.

314   Therefore, a little perturbation stemmed from human activities (e.g., agricultural

315   cultivation, coal combustion from domestic heating and cooking, and biomass burning)

316   would undoubtedly exert a considerable impact on the light absorption property.

317   A few of strong dust episodes (4, 21–22, and 30 April, 1–3, 8–11, and 20 May, 4

318   and 10 June, corresponding to DOY 95, 112–113, 121, 122–125, 129–132, 141, 156,

319   and 162) could remarkably elevate the hourly average values of PM_{10}, σ_{sp}, σ_{ap}, and

320   aerosol size distribution (see Figure 2). During these dust events, the hourly PM_{10}

321   concentrations generally exceeded 1000 μgm^{-3} and even approached 2000 μgm^{-3},

322   which were tenfold greater than the overall mean level. The hourly σ_{sp} were more

323   than 400 Mm^{-1} or even close to 800 Mm^{-1}, and the corresponding σ_{ap} varied between

324   10 Mm^{-1} and 25 Mm^{-1}. Moreover, the peak values of aerosol number size distribution

325   concentrated in the particle diameters of 1–3 μm, which was consonant with the result

326   from remote sensing (Bi et al., 2014, 2016).

327   Figure 3 depicts the time evolutions of MPL normalized relative backscatter and

328   depolarization ratio at Dunhuang farmland from 1 April to 12 June 2012. The

329   depolarization ratio (δ) is a useful indication to discriminate between spherical

330   particles (δ of ~0–0.1) and nonspherical particles (mainly dust aerosol, δ >0.2), since

331   it is very sensitive to the nonsphericity of scattering particle (Kobayashi et al., 1985;

332   Murayama et al., 1999; Shimizu et al., 2004; Huang et al., 2015). From Figure 3, we

333   can distinctly see that there was always a dense dust layer appeared at a height below

334   4 km during the whole experiment, with the peak value centered on 1.0–1.5 km,

335   which was above the planetary boundary layer (PBL). And the δ values commonly

336   reached above 0.3 (> ~0.3–0.5) during the heavy dust events and varied between 0

337   and 0.1 under clear-sky conditions (e.g., 6–7 April, 14–15 and 29 May, 9 June).

338   **3.2 Diurnal variations**

339   Figure 4 illustrates the diurnal variations of wind vector (ms^{-1}), air temperature (T

340   in ℃), RH (%), PM$_{10}$ (μgm^{-3}), $\sigma_{sp,670}$ (Mm^{-1}), $\sigma_{ap,670}$ (Mm^{-1}), aerosol number size

341   distribution (dN/dlogD in cm^{-3}), SAE at 450–700 nm, and SSA at 670 nm in

342   Dunhuang farmland from 1 April to 12 June 2012. Note that the APS spectrometer

343   was operated from 30 May to 12 June. A discernible wind vector was shown in the

344   diurnal variation, in other words, strong southwest wind and south wind dominated in

345   the daytime, from 11:00 to 24:00 LT (local time), and transformed into the weak

346   northeast wind prevailed from the midnight to the following morning of 10:00 LT.

347   The prominent phenomenon can be roughly interpreted by classical mountain-valley

348   wind circulation, which was primarily generated by the diurnal differences of

349   temperature between the mountain slope and the valley floor. During the daytime, the

350   huge Beishan Mountain slope heats up by the solar radiation more rapidly than the

351   valley floor, which causes convection above the mountain slope. The compensating

352   airflow is consequently directed toward the mountain slope, inducing upslope

353   southerly wind, or the valley wind, which usually peaks near midday and gradually

354   disappears after sunset. Conversely, at night, radiative cooling of the mountain slope

355   is more quickly than the valley floor, inducing the mountain wind, which generally

356 reaches maximum strength just before sunrise (Arya, 1999). Throughout the

357 experiment, air temperature displayed a large diurnal variation (with the diurnal

358 difference of $\delta T \sim 26$ ℃) and RH always kept below 40% for the whole day. It is very

359 clear that the minimal T and maximal RH arose at around 06:00–07:00 LT, and the

360 maximal T and minimal RH occurred at about 16:00 LT, which represented an

361 energetic vertical turbulent motion in daytime and a stable radiative temperature

362 inversion during nighttime.

363   The aerosol optical parameters also exhibited striking diurnal variations, which

364 were closely related to the local meteorological elements. During the daytime

365 (10:00–18:00 LT), the PM_{10} concentration remained high level ($\sim$57–65 μgm^{-3}) and

366 increased sharply from 19:00 LT and reached a maximum of 84.2 μgm^{-3} at 20:00 LT.

367 The PM_{10} began to decrease from 21:00 LT to the next morning. A low level ($\sim$40–46

368 μgm^{-3}) kept in the midnight (00:00–05:00 LT) and rose gradually from 06:00 LT and

369 attained a secondary peak value of 55.7 μgm^{-3} at 07:00 LT. The aerosol light

370 scattering ($\sigma_{sp,670}$) presented a similar pattern with PM_{10}, but the maximal value ($\sim$42

371 Mm^{-1}) appeared at 13:00 LT, with the other two secondary peak values occurred at

372 20:00 ($\sim$34.1 Mm^{-1}) and 07:00 LT ($\sim$27.3 Mm^{-1}). The high levels of PM_{10} and σ_{sp}

373 during the daytime were primarily attributable to strong south wind from Gobi region

374 and local dust emissions. By contrast, aerosol light absorption coefficient ($\sigma_{ap,670}$)

375 showed a more pronounced diurnal feature, which was well proved to be majorly

376 controlled by anthropogenic emissions (Li et al., 2010). The diurnal σ_{ap} always stayed

377 at a low level ($\sim$2.0 Mm^{-1}) from 13:00–18:00 LT, and also reached a maximum of 3.3

378 Mm^{-1} at 20:00 LT. Subsequently, σ_{ap} dramatically reduced from midnight and

379 preserved at a low value of about 2.2 Mm^{-1} from 02:00–04:00 LT, and remained a

380 steadily high level of $\sim$2.7–2.9 Mm^{-1} from 05:00–10:00 LT. It was probably explained

381 as follows. The influences of local anthropogenic pollutants were commonly small in

382 the afternoon, because the strong southerly wind from Gobi deserts and powerful

383 daytime vertical convection mixing efficiently dilute local air pollutants. Whereas

384 weak northeast wind and stable temperature inversion at night facilitate the

385 accumulation of pollutants within the PBL, hence nighttime levels were normally

larger. Increasing human activities (e.g., domestic cooking, traffic emissions for transportation and agriculture) in the early morning might also be responsible for the morning peaks in the aerosol absorption coefficient. The σ_{ap} maximum at 20:00 LT was presumably influenced by the mixture of mineral dust and anthropogenic pollutants. This conclusion could be partly supported by the diurnal variation of SAE at 450–700 nm (Figure 4), which showed high SAE values (~0.5–0.6) appeared at 02:00–10:00 LT and low SAE (~0.2–0.3) occurred on 13:00–22:00 LT. Generally, large SAE around 0.6 represents small particles (e.g., urban-polluted aerosol or soot) and low SAE less than 0.3 or negative value corresponds to coarse-dominated large size particles (e.g., dust or sea salt) (Anderson et al., 2003).

Furthermore, aerosol number size distribution exhibited a noticeable supermicron particles dominated in the entire day, probably linked to the predominant dust aerosol in daytime and local anthropogenic emissions at nighttime. In this study, we postulated that the aerosol light extinction at shortwave waveband is completely caused by those particles with aerodynamic diameters of 10 μm or less. And the mass scattering efficiency is designated as the ratio of σ_{sp} to PM_{10} concentration. Therefore, the mass scattering efficiency for PM_{10} aerosols was about 0.67 m^2g^{-1} in the afternoon and ~0.77 m^2g^{-1} in the morning (~0.25 for heavy dust events, and ~0.70 for the whole period). Our results were slightly less than ~1.05 m^2g^{-1} in Dunhuang during spring of 2004 (Yan, 2007). Similarly, the mass absorption efficiency was ~0.017 m^2g^{-1} under heavy dust episodes and ~0.08 m^2g^{-1} in the morning, which was coincident with the laboratory analytical result of natural desert aerosol at 660 nm (~0.01–0.02 m^2g^{-1}) in Ulan Buh desert (39°26′N, 105°40′E) of northern China (Alfaro et al., 2004). These diurnal variations of the mass scattering and absorption efficiencies likely reflect the changes in aerosol chemical composition. The SSA at 670 nm displayed distinct differences between daytime and nighttime (Figure 4), and the two minimal values at 07:00 LT (~0.90) and 20:00 LT (~0.921) were consistent with the aforementioned $\sigma_{ap,670}$ diurnal feature. The peak values of SSA (0.945±0.04) for dominant dust particles in the afternoon agreed well with other field campaigns in Zhangye (0.95±0.02, Li et al., 2010) and Yulin (0.95±0.04, Xu et al., 2004). The daily low SSA

416 (0.90–0.92) or overall mean of 0.913±0.055 at Dunhuang was still bigger than that in

417 both urban (0.81, Bergin et al., 2001) and rural regions (0.81–0.85, Li et al., 2007)

418 adjacent to Beijing, presumably ascribed to dust particles at night. Yan et al. (2008)

419 conducted two-year long field measurements at Shangdianzi Global Atmosphere

420 Watch (GAW) rural site in northern China (~150 km from Beijing) and estimated a

421 mean SSA of 0.88±0.05, but their data contained summer when aerosol scattering

422 coefficients may be strengthened by hygroscopic growth and secondary chemical

423 process.

424   The wind rose plots give a further insight into the linkages between the

425 meteorological factors and pollutants, as described in Figure 5. In the morning

426 (06:00–09:00 LT), a marked northeast wind was prevalent and wind speed was mostly

427 less than 4 ms^{-1}, which revealed that emissions were primarily descended from nearby

428 farmlands and rural residences (Figure 5a). Although a prominent northwest wind

429 mainly occurred in the evening hours (19:00–22:00 LT), the east wind and southwest

430 wind also appeared, which indicated that anthropogenic pollutions came from both

431 local sources and a relatively large region along the valley (Figure 5b). And Figure 5c

432 showed the predominant winds were northeast and southwest winds in Dunhuang area,

433 with the maximal hourly-averaged wind speed exceeding 10 ms^{-1}. It was very distinct

434 that the southwest and northwest winds created higher levels of PM_{10} mass

435 concentration (>250 μgm^{-3}), aerosol light scattering coefficient (σ_{sp} >150 Mm^{-1}) and

436 absorption coefficient (σ_{ap} >8 Mm^{-1}), whereas northeast wind generated slightly

437 smaller concentrations of PM_{10} (~50–100 μgm^{-3}), σ_{sp} (~30–60 Mm^{-1}) and σ_{ap} (~2–4

438 Mm^{-1}). This was possibly implied that southwest and northwest winds may bring

439 about dust particles and northeast wind may transport the air pollutants.

440 **3.3 Local anthropogenic emission sources**

441   As mentioned above, crop residue burning and agricultural cultivated operations

442 before the growing season could produce local emission source proximity to the study

443 area. And sporadic straw burning was indeed to happen throughout the Dunhuang

444 farmland from 1 April to 10 May 2012, which was the major source of black carbon

445 surrounding the site. To clarify the potential anthropogenic influence on aerosol

446   optical properties in desert region, we investigated a typical biomass burning event.

447   Figure 6 outlines the time series of 5-minute average wind vector (ms^{-1}), PM$_{10}$

448   (μgm^{-3}), σ$_{sp}$ at 450, 550, and 700 nm (Mm^{-1}), SAE (450–550, 550–700, and 450–700

449   nm), σ$_{ap,670}$ (Mm^{-1}), and SSA at 670 nm during a typical Tomb-sweeping Day on 4

450   April 2012. Tomb-sweeping Day is a Chinese traditional festival for sacrifice rites, in

451   commemoration of the dead ancestors. To pay homage to loved ones, the people

452   burned a lot of joss sticks, candles, and paper offerings, and set off firecrackers in that

453   day throughout the China, which would emit a great amount of air pollutants, such as,

454   biomass burning aerosol, sulfur dioxide, organic matter, and fugitive dust. From

455   Figure 6a, slight and variable winds (with wind speed <4 ms^{-1}) mainly came from

456   northeasterly from 00:00 to 12:00 LT, and abruptly changed into weak southeast wind

457   and south wind, finally, gradually intensified southwest wind (>10 ms^{-1}) were

458   predominant and triggered a severe dust storm from 15:00 LT to the midnight. Prior to

459   the occurrence of dust episode, the aerosol optical characteristics varied stably, but a

460   moderate increase was evident during 08:00 to 10:00 LT. For instance, PM$_{10}$

461   concentration gradually increased from background level ~30 μgm^{-3} to a maximum of

462   62.5 μgm^{-3} at about 09:00 LT, σ$_{sp,550}$ from ~15 Mm^{-1} to 49.6 Mm^{-1}, and σ$_{ap,670}$ from

463   ~2.0 Mm^{-1} to 4.75 Mm^{-1}. It is ascribed to the contribution of biomass burning in the

464   process of ritual activities during Tomb-sweeping Day. The SAE value at 450–700 nm

465   remained invariant (~0.50) before 08:00 LT and sharply rose to a maximal value of

466   0.87 at 09:00 LT, afterwards gently reduced to around 0.4, which indicated that the

467   fine-mode particles (i.e. black carbon or soot) were dominated from 08:00 to 10:00 LT.

468   And the SAEs at various wavelengths systematically decreased from 0.4 at 15:00 LT

469   to -0.25 at midnight, suggesting the dust-dominant coarse-mode particles were

470   prevailed. Meanwhile, the lidar depolarization ratio (δ) also further verified the

471   existence of small size soot particle. The δ value preserved steadily at 0.15–0.20

472   during 08:00 to 10:00 LT, and rapidly attained above 0.3 from 15:00 LT and even

473   approached 0.50 at intense dust storm (see Fig. 3). The diurnal variation of SSA$_{670}$

474   showed a more prominent feature, as illustrated in Figure 6f. The SSA$_{670}$ values kept

475   between 0.88 and 0.92 during 00:00 to 07:00 LT, and dramatically reduced to a

476 minimum of ~0.83 at 08:30–09:00 LT, then rose to 0.925, confirming the very striking

477 impacts by light absorbing substances. After 15:00 LT, the SSA_{670} gradually increased

478 and reached up to about 0.96 during dust storms occurred. Bi et al. (2014) have

479 demonstrated that dust aerosols shortwave radiative forcing (ARF) at the top of the

480 atmosphere (TOA) was warming effect when SSA_{500} was less than 0.85, but was

481 cooling effect when SSA_{500} was greater than 0.85 for Dunhuang Gobi desert area with

482 high surface albedo. Thereby such significant anthropogenic influence would clearly

483 modify the microphysical and chemical properties of dust aerosols and eventually

484 exert remarkable impacts on environmental quality and climatic forcing of dust

485 particle on both local and regional scales.

486 **3.4 Dust cases study**

487   In this section, we particularly explored the absorptive and optical characteristics

488 of mineral dust during several typical dust cases and discussed its influence on Earth's

489 radiation balance. Figure 7 provides the wind fields at 500 hPa and 850 hPa levels

490 during three heavy dust events, based on MERRA reanalysis products. Note that

491 Dunhuang farmland is marked with a red pentagram and the white areas at 850 hPa

492 represent the missing values. It is evident that East Asian region was governed by the

493 powerful and stable westerlies at 500 hPa height on 30 April and 1 May 2012,

494 whereas two very strong synoptic cyclones at 500 hPa upper atmosphere hovered

495 about the Mongolia and Kazakhstan respectively on 10 June 2012, matching up with

496 corresponding cyclone systems appeared at the 850 hPa level. Although there were

497 missing data in most northwest China, extremely intense northeast wind and east wind

498 (> 10 ms^{-1}) at 850 hPa level were prevailed over the northern territory of Xinjiang

499 Uygur Autonomous Region during the selected dust storms, where was close to the

500 Dunhuang site. This could be well confirmed by the simultaneous observations of

501 wind speed and wind direction nearby the surface at Dunhuang farmland, as

502 delineated in Figure 8(a). The measured strong northeast and east winds were always

503 dominated in Dunhuang and 5-min average wind speed attained above 10 ms^{-1} during

504 intense dust episodes. The selected three dust processes regularly lasted for several

505 hours during daytime (e.g., from 10:00 to 18:00 LT) and the dust event on 1 April

506 could be persistent to the midnight, which contributed massive dust particles into the
507 atmosphere.

508   There were no measurements of aerosol scattering coefficient (σ_{sp}) on 10 June due
509 to equipment failure. From Figure 8, we could know that PM_{10} concentrations usually
510 exceeded 400 μgm^{-3} and even reached up to 1000 μgm^{-3} during the heavy dust storms,
511 and corresponding $\sigma_{sp,550}$ and $\sigma_{ap,670}$ values were generally more than 100 Mm^{-1} and 5
512 Mm^{-1}, respectively, or approached 350 Mm^{-1} and 15 Mm^{-1} in our cases. It is worthy
513 note that even though pure dust aerosol possesses relatively low light-absorption
514 ability (with mass absorption efficiency at 660 nm of ~0.01–0.02 m^2g^{-1}), the injection
515 of plentiful mineral particles from dust episodes led to considerably high values of
516 $\sigma_{ap,670}$. And the SAEs at diverse wavelengths commonly kept at 0.50 or more during
517 non-dust conditions, while corresponding values dramatically reduced to -0.25~0
518 under heavy dust cases, which is taken for granted. The SSA_{670} also exhibited
519 apparent diurnal variations in Figure 8(f). The SSA_{670} values regularly preserved
520 between 0.88 and 0.92 at nighttime or non-dust weather, and gradually increased to a
521 maximum of ~0.96–0.98 during strong dust processes, which were close to the
522 measured value of ~0.97–0.99 for nearly pure Asian dust particles (Anderson et al.,
523 2003; Bi et al., 2016). These abundant mineral particles in desert source regions were
524 very likely mixed with local air pollutants especially at night, when the anthropogenic
525 pollutions favorably built up within the PBL. Moreover, airborne dust particles
526 ordinarily traveled long distances to downstream areas via synoptic cyclones, which
527 would deteriorate the ambient air quality and affected atmospheric chemistry and
528 climate change on regional scale.

529   Figure 9 describes the column-integrated aerosol optical depth (AOD) at five
530 wavelengths (400, 500, 675, 870, and 1018 nm) versus Ångström exponent (α) at
531 400–870 nm on two completely clear-sky days (14 May and 9 June) and two typical
532 dusty days (30 April and 10 June), which were acquired from sky radiometer (Model
533 POM-01, PREDE Co. Ltd.). The sky radiometer can measure the direct solar
534 irradiances and sky diffuse radiances at narrow spectral wavebands during daytime
535 with 10-minute interval. And the columnar aerosol optical properties under cloudless

conditions were retrieved from sophisticated inversion algorithms (Nakajima et al., 1996). Note that the cloud contaminated datasets have been eliminated by means of a series of cloud screening procedures developed by Khatri and Takamura (2009). From Figure 9, all AOD values under clear-sky days kept very stable variations throughout the day and ranged from 0.02 to 0.12, which were comparable to the clean background levels in the central Tibetan Plateau (Xia et al., 2011) and Badain Jaran Desert (Bi et al., 2013). And the corresponding Ångström exponent α on 14 May and 9 June were greater than 0.6, indicating extremely low aerosol loading. In contrast, the AODs under dust events (30 April and 10 June) displayed pronounced diurnal variations and all AOD values were larger than 0.30 (with maximum of 0.60), and α varied between 0.10 and 0.25, representing high dust concentration levels. These elevated dust particles in the atmosphere would readjust the energy distributions of solar radiative fluxes at the surface.

Based on aforementioned measurements of total sky imager, micro-pulse lidar and sky radiometer, we identified three completely clear-sky days (14 May, 29 May, and 9 June) and two "clean" dusty days (30 April and 10 June). The "clean" dusty days in this study were denoted as the dust storms weather without the influence of clouds. This afforded us a good opportunity to elucidate the potential impacts of dust events on radiation balance at the ground. Figure 10 draws the 1-minute average solar direct normal radiation, sky diffuse radiation, total shortwave radiation, and downward long-wave radiation fluxes under the selected five days, which were derived from the high-precision broadband radiometers as described in section 2.3. All radiative quantities presented smooth diurnal variations under clear-sky cases (14 May, 29 May, and 9 June). The airborne dust particles impeded the sunlight to the ground through scattering and absorbing solar radiation, for instance, they could significantly reduced the surface direct radiative fluxes in daytime about 200–350 Wm^{-2} (Figure 10a), whereas considerably increased the surface diffuse radiative fluxes up to ~150–300 Wm^{-2} (Figure 10b). As a result, the overall attenuation effect on total shortwave radiative fluxes varied between –150 and –50 Wm^{-2}. The incoming solar energy absorbed by dust particles would heat the atmospheric dust layer (Bi et al., 2014) that

likely played a profound role in the structure of atmospheric boundary layer and cloud microphysical process (J. Huang et al., 2006, 2010; Li et al., 2016). The downward longwave radiation (DLW) at the surface was majorly reliant on the clouds, water vapor, CO_2, and other greenhouse gases (Wang and Dickinson, 2013). In general, the presence of clouds in the atmosphere would fluctuate drastically the diurnal variation of DLW. And the smooth changes of DLW under both clear-sky and dusty days in Figure 10d revealed the robustness of the cloud screening method used in this paper. Figure 10d displays that the DLW values under dusty cases were always greater than that in clear-sky cases, with the total average differences of +40~+60 Wm^{-2}. The warming dust layer could enhance the surface DLW, hence the dust particles should contribute a large percentages to the increased DLW, but not all. This is because the potential water vapor in the atmosphere could substantially affect the DLW variations. For instance, the DLW on 9 June were distinctly larger than that in other cloudless cases (i.e., 14 and 29 May) and the dusty case of 30 April. It is partly attributable to the higher RH values on 9 June than that in other days, as shown in Figure S2.

4. Concluding remarks

In this article, we surveyed the optical features and size distribution of dust aerosol in a Gobi farmland region of northwest China from 1 April to 12 June 2012, and uncovered a potential anthropogenic influence. The overall average PM_{10} mass concentration, light scattering coefficient ($\sigma_{sp,670}$), absorption coefficient ($\sigma_{ap,670}$), and single-scattering albedo (SSA_{670}) throughout the experiment were 113±169 μgm^{-3}, 53.3±74.8 Mm^{-1}, 3.2±2.4 Mm^{-1}, and 0.913±0.05, which were comparable to the background levels in southern United States, but lower than that in the eastern and other northwestern China. Frequent dust storms could markedly elevate dust loading and dominated the temporal evolution of airborne aerosol in Dunhuang region. The hourly average PM_{10}, $\sigma_{sp,670}$, and $\sigma_{ap,670}$ reached up to 2000 μgm^{-3}, 800 Mm^{-1}, and 25 Mm^{-1} during the severe dust events that were tenfold greater than the total mean values, along with the particle size concentrated in diameters of 1–3 μm. Meanwhile, the correspondingly high SSA_{670} (~0.96–0.98) and depolarization ratio (δ of ~0.3–0.5),

595   and low SAE (-0.25~0) values adequately verified the presence of coarse-mode

596   mineral dust, resulting in significantly reducing the solar direct radiation (~200–350

597   Wm^{-2}) and increasing diffuse radiation (~150–300 Wm^{-2}) at the surface, and hence

598   affecting the regional climate.

599   Owing to relatively low aerosol levels observed in Dunhuang, any slightly

600   anthropogenic perturbation would induce a substantial influence on the aerosol

601   physicochemical property. The so-called anthropogenic dust produced by agricultural

602   cultivating operations (e.g., land planning, plowing, and disking) brought a significant

603   superimposed effect on high dust concentrations in Dunhuang farmland prior to the

604   growing season, when the underlying surface was primarily covered with bare soils.

605   This to some extent could be interpreted the drastic changes of aerosol loadings in

606   April and early May. In contrast, the local pollutant emissions mainly affected the

607   absorptive characteristics of dust aerosol especially at night, when the anthropogenic

608   pollutants favorably accumulated within the PBL and likely mixed with abundant

609   mineral dust in the atmosphere. Therefore, the diurnal variations of $\sigma_{ap,670}$ and SSA_{670}

610   exhibited prominent features, both of which have got two peak values at night and in

611   the early morning. For instance, ~3.3 Mm^{-1} at 20:00 LT and ~2.9 Mm^{-1} at 08:00 LT

612   for $\sigma_{ap,670}$ were much more than the low level of ~2.0 Mm^{-1} in the afternoon, which

613   was attributed to the influence of anthropogenic emissions. And the mean SSA_{670} of

614   predominant dust particles in the afternoon (13:00–18:00 LT) was 0.945±0.04 that

615   was evidently greater than the mixed dust-pollutants dominated SSA_{670} of ~0.90 at

616   07:00 LT and ~0.92 at 20:00 LT.

617   The findings of this study directly demonstrated that mineral dust in Dunhuang

618   farmland was substantially affected by anthropogenic pollutants, which would help to

619   promote a further insight into the interaction among dust aerosol, atmospheric

620   chemistry, and regional climate in desert source region. However, the potentially

621   anthropogenic influences on dust aerosol in Dunhuang showed far smaller than that

622   measured in eastern China, which was expected for the remote desert areas with

623   sparsely population and lesser human activities. Recently, Huang et al. (2016)

624   indicated that most of the drylands in the world were fragile and susceptible to climate

change and human activities and would be subject to the acceleration of drought expansion by the end of twenty-first century. Under the possible scenario, it is very critical to make clear the relative contributions of natural and anthropogenic forcing factors on global climate change, such as, natural dust and anthropogenic dust, which calls for further investigating through a lot more observations and technologies.

5. Data availability

All ground-based aerosol datasets used in this paper are available via contacting Jianrong Bi (bijr@lzu.edu.cn).

Acknowledgements. This work was jointly supported by the Foundation for Innovative Research Groups of the National Natural Science Foundation of China (41521004), the National Natural Science Foundation of China (41575015 and 41405113), the Fundamental Research Funds for the Central Universities lzujbky-2015-4 and lzujbky-2016-k01, and the China 111 Project (No. B 13045). The authors would like to express special thanks to David S. Covert for guiding the in-situ aerosol measurements. We thank the OMI and MERRA teams for supplying the satellite data and reanalysis products used in this study. We also appreciate all anonymous reviewers for their insightful and valuable comments.

References

Alfaro, S. C., Lafon, S., Rajot, J. L., Formenti, P., Gaudichet, A., and Maillé, M.: Iron oxides and light absorption by pure desert dust: An experimental study, J. Geophys. Res., 109, D08208, doi:10.1029/2003JD004374, 2004.

Anderson, T. L., Covert, D. S., Marshall, S. F., Laucks, M. L., Charlson, R. J., Waggoner, A. P., Ogren, J. A., Caldow, R., Holm, R. L., Quant, F. R., Sem, G. J., Wiedensohler, A., Ahlquist, N. A., and Bates, T. S.: Performance characteristics of a high–sensitivity, three–wavelength total scatter–backscatter nephelometer, J. Atmos. Oceanic Technol., 13: 967–986, 1996.

Anderson, T. L. and Ogren, J. A.: Determining aerosol radiative properties using the TSI 3563 Integrating Nephelometer, Aerosol Sci. Technol., 29, 57–69, doi:10.1080/02786829808965551, 1998.

654 Anderson, T. L., Masonis, S. J., Covert, D. S., Ahlquist, N. C., Howell, S. G., Clarke, A. D., and

655   McNaughton, C. S.: Variability of aerosol optical properties derived from in situ aircraft

656   measurements during ACE–Asia, J. Geophys. Res., 108(D23), 8647,

657   doi:10.1029/2002JD003247, 2003.

658 Aoki, I., Kurosaki, Y., Osada, R., Sato, T., and Kimura, F.: Dust storms generated by mesoscale

659   cold fronts in the Tarim Basin, Northwest China, Geophys. Res., Lett., 32, L06807,

660   doi:10.1029/2004GL021776, 2005.

661 Aoki, T., Motoyoshi, H., Kodama, Y., Yasunari, T. J., Sugiura, K., and Kobayashi, H.:

662   Atmospheric aerosol deposition on snow surfaces and its effect on albedo, SOLA, 2, 13–16,

663   doi:10.2151/sola.2006–004, 2006.

664 Arimoto, R., Zhang, X. Y., Huebert, B .J., Kang, C. H., Savoie, D. L., Prospero, J. M., Sage, S. K.,

665   Schloesslin, C. A., Khaing, H. M., and Oh, S. N.: Chemical composition of atmospheric

666   aerosols from Zhenbeitai, China, and Gosan, South Korea, during ACE–Asia, J. Geophys. Res.,

667   109, D19S04, doi:10.1029/2003JD004323, 2004.

668 Arimoto, R., Kim, Y. J., Kim, Y. P., Quinn, P. K., Bates, T. S., Anderson, T. L., Gong, S., Uno, I.,

669   Chin, M., Huebert, B. J., Clarke, A. D., Shinozuka, Y., Weber, R. J., Anderson, J. R., Guazzotti,

670   S. A., Sullivan, R. C., Sodeman, D. A., Prather, K. A., and Sokolik, I. N.: Characterization of

671   Asian dust during ACE–Asia, Global Planet. Change, 52, 23–56,

672   doi:10.1016/j.gloplacha.2006.02.013, 2006.

673 Arya, S. P.: Air Pollution Meteorology and Dispersion, 310 pp., Oxford University Press, New

674   York, 1999.

675 Bergin, M. H., Cass, G. R., Xu, J., Fang, C., Zeng, L. M., Yu, T., Salmon, L. G., Kiang, C. S., Tang,

676   X. Y., Zhang, Y. H., and Chameides, W. L.: Aerosol radiative, physical, and chemical properties

677   in Beijing during June 1999, J. Geophys. Res., 106(D16), 17969–17980, doi:

678   10.1029/2001JD900073, 2001.

679 Bi, J., Huang, J., Fu, Q., Wang, X., Shi, J., Zhang, W., Huang, Z., and Zhang B.: Toward

680   characterization of the aerosol optical properties over Loess Plateau of Northwestern China, J.

681   Quant. Spectrosc. Radiat. Transfer., 112, 346–360, doi:10.1016/j.jqsrt.2010.09.006, 2011.

682 Bi, J., Huang, J., Fu, Q., Ge, J., Shi, J., Zhou, T., and Zhang, W.: Field measurement of clear–sky

683   solar irradiance in Badain Jaran Desert of Northwestern China, J. Quant. Spectroc. Radiat.

Transf., 122, 194–207, doi:10.1016/j.jqsrt.2012.07.025, 2013.

Bi, J., Shi, J., Xie, Y., Liu, Y., Takamura, T., and Khatri, P.: Dust aerosol characteristics and shortwave radiative impact at a Gobi Desert of Northwest China during the spring of 2012, J. Meteor. Soc. Jpn, Ser. II, 92A, 33–56, DOI:10.2151/jmsj.2014–A03, 2014.

Bi, J., Huang, J., Holben, B., and Zhang, G.: Comparison of key absorption and optical properties between pure and transported anthropogenic dust over East and Central Asia, Atmos. Chem. Phys., 16, 15501–15516, doi:10.5194/acp–16–15501–2016, 2016.

Campbell, J. R., Hlavka, D. L., Welton, E. J., Flynn, C. J., Turner, D. D., Spinhirne, J. D., Scott, V. S., and Hwang, I. H.: Full-Time, eye-safe cloud and aerosol lidar observation at Atmospheric Radiation Measurement program sites: Instruments and data processing, J. Atmos. Oceanic Technol., 19, 431–442, doi:10.1175/1520-0426(2002)019<0431:FTESCA>2.0.CO;2, 2002.

Cao, J. J., Lee, S. C., Zhang, X. Y., Chow, J. C., An, Z. S., Ho, K. F., Watson, J. G., Fung, K., Wang, Y. Q., and Shen, Z. X.: Characterization of airborne carbonate over a site on Asian dust source regions during 2002 spring and its climatic and environmental significance, J. Geophys. Res., 110, D03203, doi:10.1029/2004JD005244, 2005.

Che, H., Zhang, X. Y., Chen, H. B., Damiri, B., Goloub, P., Li, Z., Zhang, X., Wei, Y., Zhou, H., Dong, F., Li, D., and Zhou, T.: Instrument calibration and aerosol optical depth validation of the China Aerosol Remote Sensing Network, J. Geophys. Res., 114, D03206, doi:10.1029/2008JD011030, 2009.

Che, H., Zhang, X.–Y., Xia, X., Goloub, P., Holben, B., Zhao, H., Wang, Y., Zhang, X.–C., Wang, H., Blarel, L., Damiri, B., Zhang, R., Deng, X., Ma, Y., Wang, T., Geng, F., Qi, B., Zhu, J., Yu, J., Chen, Q., and Shi, G.: Ground–based aerosol climatology of China: aerosol optical depths from the China Aerosol Remote Sensing Network (CARSNET) 2002–2013, Atmos. Chem. Phys., 15, 7619–7652, doi:10.5194/acp–15–7619–2015, 2015.

Cheng, T., Lu, D., Wang, G., and Xu, Y.: Chemical characteristics of Asian dust aerosol from Hunshan Dake Sandland in Northern China, Atmos. Environ., 39, 2903–2911, doi:10.1016/j.atmosenv.2004.12.045, 2005.

Covert, D. S., Charlson, R. J., and Ahlquist, N. C.: A study of the relationship of chemical composition and humidity to light scattering by aerosols, J. Appl. Meteo., 11: 968–976, 1972.

Creamean, J. M., Suski, K. J., Rosenfeld, D., Cazorla, A., DeMott, P. J., Sullivan, R. C., White, A.

714   B., Ralph, F. M., Minnis, P., Comstock, J. M., Tomlinson, J. M., and Prather, K. A.: Dust and

715   biological aerosols from the Sahara and Asia influence precipitation in the western U.S.,

716   Science, 339, 1572–1578, doi:10.1126/science.1227279, 2013.

717   Delene, D. and Ogren, J. A.: Variability of aerosol optical properties at four North American

718   surface   monitoring   sites,   J.   Atmos.   Sci.,   59(6),   1135–1150,

719   doi:10.1175/1520-0469(2002)059<1135:VOAOPA>2.0.CO;2, 2002.

720   Dubovik, O., Holben, B. N., Eck, T. F., Smirnov, A., Kaufman, Y. J., King, M. D., Tanré, D., and

721   Slutsker, I.: Variability of absorption and optical properties of key aerosol types observed in

722   worldwide locations, J. Atmos. Sci., 59, 590–608, 2002.

723   Eck, T. F., Holben, B. N., Dubovik, O., Smirnov, A., Goloub, P., Chen, H. B., Chatenet, B., Gomes,

724   L., Zhang, X.-Y, Tsay, S.-C., Ji, Q., Giles, D., and Slutsker, I.: Columnar aerosol optical

725   properties at AERONET sites in central eastern Asia and aerosol transport to the tropical

726   mid-Pacific, J. Geophys. Res., 110, D06202, doi:10.1029/2004JD005274, 2005.

727   Ge, J., Su, J., Ackerman, T. P., Fu, Q., Huang, J., and Shi, J.: Dust aerosol optical properties

728   retrieval and radiative forcing over northwest China during the 2008 China–U.S. joint field

729   experiment, J. Geophys. Res., 115, D00K12, doi:10.1029/2009JD013263, 2010.

730   Ge, J., Liu, H., Huang, J., and Fu, Q.: Taklimakan Desert nocturnal low-level jet: climatology and

731   dust activity, Atmos. Chem. Phys., 16, 7773–7783, doi:10.5194/acp-16-7773-2016, 2016.

732   Ginoux, P., Prospero, J. M., Gill, T. E., Hsu, N. C., and Zhao, M.: Global–scale attribution of

733   anthropogenic and natural sources and their emission rates based on MODIS Deep Blue aerosol

734   products, Rev. Geophys., 50, RG3005, doi:10.1029/2012RG000388, 2012.

735   Guan, X., Huang, J., Zhang, Y., Xie, Y., and Liu, J.: The relationship between anthropogenic dust

736   and population over global semi–arid regions, Atmos. Chem. Phys., 16, 5159–5169,

737   doi:10.5194/acp–16–5159–2016, 2016.

738   Hansen, J., Sato, M., and Ruedy, R.: Radiative forcing and climate response, J. Geophys. Res., 102,

739   6831–6864, 1997.

740   Holben, B. N., Eck, T. F., Slutsker, I., Tanre, D., Buis, J. P., Setzer, A., Vermote, E., Reagan, J. A.,

741   Kaufman, Y. J., Nakajima, T., Lavenu, F., Jankowiak, F., and Smirnov, A., AERONET—A

742   federated instrument network and data archive for aerosol characterization, Remote Sens.

743   Environ., 66, 1–16, 1998.

744   Huang, J., Minnis, P., Lin, B., Yi, Y., Khaiyer, M. M., Arduini, R. F., Fan, A., and Mace, G. G.:

745   Advanced retrievals of multilayered cloud properties using multispectral measurements, J.

746   Geophys. Res., 110, D15S18, doi:10.1029/2004JD005101, 2005.

747   Huang, J., Lin, B., Minnis, P., Wang, T., Wang, X., Hu, Y., Yi, Y., and Ayers, J. K.: Satellite–based

748   assessment of possible dust aerosols semi–direct effect on cloud water path over East Asia,

749   Geophys. Res. Lett., 33, L19802, doi:10.1029/2006GL026561, 2006.

750   Huang, J., Minnis, P., Chen, B., Huang, Z., Liu, Z., Zhang, Q., Yi, Y., and Ayers, J. K.: Long–range

751   transport and vertical structure of Asian dust from CALIPSO and surface measurements during

752   PACDEX, J. Geophys. Res., 113, D23212, doi:10.1029/2008JD010620, 2008a.

753   Huang, J., Zhang, W., Zuo, J., Bi, J., Shi, J., Wang, X., Chang, Z., Huang, Z., Yang, S., Zhang, B.,

754   Wang, G., Feng, G., Yuan, J., Zhang, L., Zuo, H., Wang, S., Fu, C., and Chou, J.: An overview of

755   the semi–arid climate and environment research observatory over the Loess Plateau, Adv.

756   Atmos. Sci., 25, 906–921, doi:10.1007/s00376–008–0906–7, 2008b.

757   Huang, J., Fu, Q., Su, J., Tang, Q., Minnis, P., Hu, Y., Yi, Y., and Zhao, Q.: Taklimakan dust

758   aerosol radiative heating derived from CALIPSO observations using the Fu–Liou radiation

759   model with CERES constraints, Atmos. Chem. Phys., 9, 4011–4021,

760   doi:10.5194/acp–9–4011–2009, 2009.

761   Huang, J., Minnis, P., Yan, H., Yi, Y., Chen, B., Zhang, L., and Ayers, J. K.: Dust aerosol effect on

762   semi–arid climate over Northwest China detected from A–Train satellite measurements, Atmos.

763   Chem. Phys., 10, 6863–6872, doi:10.5194/acp–10–6863–2010, 2010.

764   Huang, J., Fu, Q., Zhang, W., Wang, X., Zhang, R., Ye, H., and Warren, S. G.: Dust and black

765   carbon in seasonal snow across northern China, Bull. Amer. Meteor. Soc., 92, 175–181,

766   doi:10.1175/2010BAMS3064.1, 2011.

767   Huang, J., Wang, T., Wang, W., Li, Z., and Yan, H.: Climate effects of dust aerosols over East

768   Asian arid and semiarid regions, J. Geophys. Res., 119, 11398–11416,

769   doi:10.1002/2014JD021796, 2014.

770   Huang, J. P., Liu, J. J., Chen, B., and Nasiri, S. L.: Detection of anthropogenic dust using

771   CALIPSO lidar measurements, Atmos. Chem. Phys., 15, 11653–11665,

772   doi:10.5194/acp–15–11653–2015, 2015.

773   Huang, J., Yu, H., Guan, X., Wang, G., and Guo, R.: Accelerated dryland expansion under climate

774   change, Nature Clim. Change, 6(2), 166–171, doi:10.1038/nclimate2837, 2016.

775   Huang, K., Zhuang, G., Li, J., Wang, Q., Sun, Y., Lin, Y., and Fu, J. S.: Mixing of Asian dust with

776   pollution aerosol and the transformation of aerosol components during the dust storm over

777   China in spring 2007, J. Geophys. Res., 115, D00K13, doi:10.1029/2009JD013145, 2010.

778   Huang, Z., Huang, J., Bi, J., Wang, G., Wang, W., Fu, Q., Li, Z., Tsay, S.–C., and Shi, J.: Dust

779   aerosol vertical structure measurements using three MPL lidars during 2008 China–U.S. joint

780   dust field experiment, J. Geophys. Res., 115, D00K15, doi:10.1029/2009JD013273, 2010.

781   Huebert, B. J., Bates, T., Russell, P. B., Shi, G., Kim, Y. J., Kawamura, K., Carmichael, G., and

782   Nakajima, T.: An overview of ACE–Asia: Strategies for quantifying the relationships between

783   Asian aerosols and their climatic impacts, J. Geophys. Res., 108(D23), 8633,

784   doi:10.1029/2003JD003550, 2003.

785   Intergovernmental Panel on Climate Change (IPCC): *Climate Change 2013: The Physical Science*

786   *Basis, Contribution of Working Group I to the Fifth Assessment Report of the Intergovernmental*

787   *Panel on Climate Change,* edited by Stocker, T. F., D. Qin, G. –K. Plattner, M. Tignor, S. K.

788   Allen, J. Boschung, A. Nauels, Y. Xia, V. Bex and P. M. Midgley. Cambridge University Press,

789   Cambridge, United Kingdom and New York, NY, USA, 1535 pp, 2013.

790   Jickells, T., An, Z., Andersen, K., Baker, A., Bergametti, G., Brooks, N., Cao, J., Boyd, P., Duce,

791   R., Hunter, K., Kawahata, H., Kubilay, N., laRoche, J., Liss, P., Mahowald, N., Prospero, J.,

792   Ridgwell, A., Tegen, I., and Torres, R.: Global iron connections between desert dust, ocean

793   biogeochemistry, and climate, Science, 308, 67–71, doi:10.1126/science.1105959, 2005.

794   Kai, K., Nagata, Y., Tsunematsu, N., Matsumura, T., Kim, H.–S., Matsumoto, T., Hu, S., Zhou, H.,

795   Abo, M., and Nagai, T.: The structure of the dust layer over the Taklimakan Desert during the

796   dust storm in April 2002 as observed using a depolarization lidar, J. Meteor. Soc. Jpn, 86(1),

797   1–16, doi:10.2151/jmsj.86.1, 2008.

798   Khatri, P. and Takamura, T.: An algorithm to screen cloud-affected data for sky radiometer data

799   analysis, J. Meteor. Soc. Jpn, 87, 189–204, doi:10.2151/jmsj.87.189, 2009.

800   Kobayashi, A., Hayashida, S., Okada, K., and Iwasaka, Y.: Measurements of the polarization

801   properties of Kosa (Asian Dust storm) particles by a Laser Radar in spring 1983, J. Meteor. Soc.,

802   Jpn., 63, 144–149, 1985.

803   Lafon, S., Rajot, J.–L., Alfaro, S. C., and Gaudichet, A.: Quantification of iron oxides in desert

804   aerosol, Atmos. Environ., 38, 1211–1218, 2004.

805 Lafon, S., Sokolik, I. N., Rajot, J. L., Caquineau, S., and Guadichet, A.: Characterization of iron

806   oxides in mineral dust aerosols: Implications for light absorption, J. Geophys. Res., 111,

807   D21207, doi:10.1029/2005JD007016, 2006.

808 Li, C., Marufu, L. T., Dickerson, R. R., Li, Z., Wen, T., Wang, Y., Wang, P., Chen, H., and Stehr, J.

809   W.: In situ measurements of trace gases and aerosol optical properties at a rural site in northern

810   China during East Asian Study of Tropospheric Aerosols: An International Regional Experiment

811   2005, J. Geophys. Res., 112, D22S04, doi:10.1029/2006JD007592, 2007.

812 Li, C., Tsay, S.–C., Fu, J. S., Dickerson, R. R., Ji, Q., Bell, S. W., Gao, Y., Zhang, W., Huang, J., Li,

813   Z., and Chen, H.: Anthropogenic air pollution observed near dust source regions in

814   northwestern China during springtime 2008, J. Geophys. Res., 115, D00K22,

815   doi:10.1029/2009JD013659, 2010.

816 Li, W. J. and Shao, L. Y.: Observation of nitrate coatings on atmospheric mineral dust particles,

817   Atmos. Chem. Phys., 9, 1863–1871, doi:10.5194/acp-9-1863-2009, 2009.

818 Li, Z., Li, C., Chen, H., Tsay, S.–C., Holben, B., Huang, J., Li, B., Maring, H., Qian, Y., Shi, G.,

819   Xia, X., Yin, Y., Zheng, Y., and Zhuang, G.: East Asian Studies of Tropospheric Aerosols and

820   their Impact on Regional Climate (EAST–AIRC): An overview, J. Geophys. Res., 116, D00K34,

821   doi:10.1029/2010JD015257, 2011.

822 Li, Z., Lau, W. K.–M., Ramanathan, V., Wu, G., Ding, Y., Manoj, M. G., Liu, J., Qian, Y., Li, J.,

823   Zhou, T., Fan, J., Rosenfeld, D., Ming, Y., Wang, Y., Huang, J., Wang, B., Xu, X., Lee, S.–S.,

824   Gribb, M., Zhang, F., Yang, X., Zhao, C., Takemura, T., Wang, K., Xia, X., Yin, Y., Zhang, H.,

825   Guo, J., Zhai, P. M., Sugimoto, N., Babu, S. S., and Brasseur, G. P.: Aerosol and monsoon

826   climate interactions over Asia, Rev. Geophys., 54, doi:10.1002/2015RG000500, 2016.

827 Ma, J., He, J., Qi, S., Zhu, G., Zhao, W., Edmunds, W. M., and Zhao, Y.: Groundwater recharge

828   and evolution in the Dunhuang Basin, northwestern China, Appl. Geochem., 28, 19–31,

829   doi:10.1016/j.apgeochem.2012.10.007, 2013.

830 Maher, B. A., Prospero, J. M., Mackie, D., Gaiero, D., Hesse, P. P., and Balkanski, Y.: Global

831   connections between aeolian dust, climate and ocean biogeochemistry at the present day and at

832   the last glacial maximum, Earth–Sci. Rev., 99 (1–2), pp. 61–97,

833   doi:10.1016/j.earscirev.2009.12.001, 2010.

834   Mikami, M., Shi, G. Y., Uno, I., Yabuki, S., Iwasaka, Y., Yasui, M., Aoki, T., Tanaka, T. Y.,

835   Kurosaki, Y., Masuda, K., Uchiyama, A., Matsuki, A., Sakai, T., Takemi, T., Nakawo, M., Seino,

836   N., Ishizuka, M., Satake, S., Fujita, K., Hara, Y., Kai, K., Kanayama, S., Hayashi, M., Du, M.,

837   Kanai, Y., Yamada, Y., Zhang, X. Y., Shen, Z., Zhou, H., Abe, Q., Nagai, T., Tsutsumi, Y. , Chiba,

838   M., and Suzuki, J.: Aeolian dust experiment on climate impact: An overview of Japan–China

839   joint project ADEC, Global Planet. Change, 52, 142–172, doi:10.1016/j.gloplacha.2006.03.001,

840   2006.

841   Murayama, T., Okamoto, H., Kaneyasu, N., Kamataki, H., and Miura, K.: Application of lidar

842   depolarization measurement in the atmospheric boundary layer: Effects of dust and sea-salt

843   particles, J. Geophys. Res., 104, 31781–31792, 1999.

844   Nakajima, T., Tonna, G., Rao, R., Boi, P., Kaufman, Y., and Holben, B.: Use of sky brightness

845   measurements from ground for remote sensing of particulate polydispersions, Appl. Opt.,

846   35(15), 2672–2686, doi:10.1364/AO.35.002672, 1996.

847   Nakajima, T., Sekiguchi, M., Takemura, T., Uno, I., Higurashi, A., Kim, D., Sohn, B. J., Oh, S.

848   –N., Nakajima, T. Y., Ohta, S., Okada, I., Takamura, T, and Kawamoto, K.: Significance of

849   direct and indirect radiative forcings of aerosols in the East China Sea region, J. Geophys. Res.,

850   108(D23), 8658, doi:10.1029/2002JD003261, 2003.

851   Nie, W., Ding, A., Wang, T., Kerminen, V.-M., George, C., Xue, L., Wang, W., Zhang, Q., Petäjä,

852   T., Qi, X., Gao, X., Wang, X., Yang, X., Fu, C., and Kulmala, M.: Polluted dust promotes new

853   particle formation and growth, Sci. Rep., 4: 6634, DOI:10.1038/srep06634, 2014.

854   Petzold, A., Kramer, H., and Schönlinner, M.: Continuous measurement of atmospheric black

855   carbon using a multi‑angle absorption photometer, Environ. Sci. Poll. Res., 4: 78–82, 2002.

856   Petzold, A., Schloesser, H., Sheridan, P. J., Arnott, W. P., Ogren, J. A., and Virkkula A.: Evaluation

857   of multiangle absorption photometry for measuring aerosol light absorption, Aerosol Sci. Tech.,

858   39:1, 40–51, doi:10.1080/027868290901945, 2005.

859   Qian, Y., Yasunnari, T. J., Doherty, S. J., Flanner, M. G., Lau, W. K.–M., Ming, J., Wang, H., Wang,

860   M., Warren, S. G., and Zhang, R.: Light–absorbing particles in snow and ice: Measurement and

861   modeling of climatic and hydrological impact, Adv. Atmos. Sci., 32, 64–91,

862   doi:10.1007/s00376-014-0010-0, 2014.

863   Ramanathan, V., Crutzen, P. J., Kiehl, J. T., and Rosenfeld, D.: Aerosols, climate, and the

864   hydrological cycle, Science, 294, 2119–2124, doi:10.1126/science.1064034, 2001.

865   Rienecker, M. M., Suarez, M. J., Gelaro, R., Todling, R., Bacmeister, J., Liu, E., Bosilovich, M. G.,

866   Schubert, S. D., Takacs, L., Kim, G.-K., Bloom, S., Chen, J., Collins, D., Conaty, A., Silva, A.

867   da, Gu, W., Joiner, J., Koster, R. D., Lucchesi, R., Molod, A., Owens, T., Pawson, S., Pegion, P.,

868   Redder, C. R., Reichle, R., Robertson, F. R., Ruddick, A. G., Sienkiewicz, M., and Woollen, J.:

869   MERRA: NASA's Modern–Era Retrospective Analysis for Research and Applications, J.

870   Climate, 24, 3624–3648. doi: 10.1175/JCLI-D-11-00015.1, 2011.

871   Rosenfeld, D., Rudich, Y., and Lahav, R.: Desert dust suppressing precipitation: A possible

872   desertification feedback loop, Proc. Natl. Acad. Sci. U.S.A., 98, 5975–5980, 2001.

873   Shao, Y., Wyrwoll, K.–H., Chappel, A., Huang, J., Lin, Z., McTainsh, G., Mikami, M., Tanaka, T.,

874   Wang, X., and Yoon, S.: Dust cycle: An emerging core theme in Earth system science, Aeolian

875   Res., 2, 181–204, 2011.

876   Shimizu, A., Sugimoto, N., Matsui, I., Arao, K., Uno, I., Murayama, T., Kagawa, N., Aoki, K.,

877   Uchiyama, A., and Yamazaki, A.: Continuous observations of Asian dust and other aerosol by

878   polarization lidars in China and Japan during ACE-Asia, J. Geophys. Res., 109, D19S17,

879   doi:10.1029/2002JD003253, 2004.

880   Sokolik, I. N. and Toon, O. B.: Incorporation of mineralogical composition into models of the

881   radiative properties of mineral aerosol from UV to IR wavelengths, J. Geophys. Res., 104, D8,

882   9423–9444, 1999.

883   Sun, J., Zhang, M., and Liu, T.: Spatial and temporal characteristics of dust storms in China and its

884   surrounding regions, 1960–1990: Relations to source area and climate, J. Geophys. Res.,

885   106(D10), 10325–10333, doi:10.1029/2000JD900665, 2001.

886   Takamura, T., Nakajima, T., and SKYNET community group: Overview of SKYNET and its

887   Activities, Opt. Puray Apl., 37, 3303–3308, 2004.

888   Tegen, I. and Fung, I.: Contribution to the atmospheric mineral aerosol load from land surface

889   modification, J. Geophys. Res., 100, 18707–18726, doi:10.1029/95JD02051, 1995.

890   Torres, O., Tanskanen, A., Veihelmann, B., Ahn, C., Braak, R., Bhartia, P. K., Veefkind, P., and

891   Levelt, P.: Aerosols and surface UV products from Ozone Monitoring Instrument observations:

892   An overview, J. Geophys. Res., 112, D24S47, doi:10.1029/2007JD008809, 2007.

893   Uchiyama, A., Yamazaki, A., Togawa, H., Asano, J., and Shi, G.–Y.: Single scattering albedo of

894   Aeolian dust as inferred from sky–radiometer and in situ ground–based measurement, SOLA,

895   Vol. 1, pp. 209–212, doi:10.2151/sola.2005–054, 2005.

896   Uno, I., Eguchi, K., Yumimoto, K., Takemura, T., Shimizu, A., Uematsu, M., Liu, Z., Wang, Z.,

897   Hara, Y., and Sugimoto, N.: Asian dust transported one full circuit around the globe, Nature

898   Geosci., 2, 557–560, doi:10.1038/NGEO583, 2009.

899   Uno,I., Eguchi, K., Yumimoto, K., Liu, Z., Hara, Y., Sugimoto, N., Shimizu, A., and Takemura, T.:

900   Large Asian dust layers continuously reached North America in April 2010, Atmos. Chem.

901   Phys., 11, 7333–7341, 2011.

902   Wang, G., Huang, J., Guo, W., Zuo, J., Wang, J., Bi, J., Huang, Z., and Shi, J.: Observation

903   analysis of land–atmosphere interactions over the Loess Plateau of northwest China, J. Geophys.

904   Res., 115, D00K17,doi:10.1029/2009JD013372, 2010.

905   Wang, K., and Dickinson, R. E.: Global atmospheric downward longwave radiation at the surface

906   from ground-based observations, satellite retrievals, and reanalyses, Rev. Geophys., 51,

907   150–185, doi:10.1002/rog.20009, 2013.

908   Wang, W., Huang, J., Minnis, P., Hu, Y., Li, J., Huang, Z., Ayers, J. K., and Wang, T.: Dusty cloud

909   properties and radiative forcing over dust source and downwind regions derived from A–Train

910   data during the Pacific Dust Experiment, J. Geophys. Res., 115, D00H35,

911   doi:10.1029/2010JD014109, 2010.

912   Wang, X., Huang, J., Ji, M., and Higuchi, K.: Variability of East Asia dust events and their

913   long–term trend, Atmos. Environ., 42, 13, 3156–3165, doi:10.1016/j.atmosenv.2007.07.046,

914   2008.

915   Wang, X., Doherty, S. J., and Huang, J.: Black carbon and other light–absorbing impurities in

916   snow across Northern China, J. Geophys. Res., 118, 1471–1492, doi:10.1029/2012JD018291,

917   2013.

918   Wang, X., Pu, W., Shi, J., Bi, J., Zhou, T., Zhang, X., and Ren, Y.: A comparison of the physical

919   and optical properties of anthropogenic air pollutants and mineral dust over Northwest China, J.

920   Meteorol. Res., 29, 180–200, doi:10.1007/s13351–015–4092–0, 2015.

921   Welton, E. J., Voss, K. J., Gordon, H. R., Maring, H., Smirnov, A., Holben, B., Schmid, B.,

922   Livingston, J. M., Russell, P. B., Durkee, P. A., Formenti, P., and Andreae, M. O.: Ground-based

923   lidar measurements of aerosols during ACE-2: Instrument description, results, and comparisons

924   with other ground-based and airborne measurements, Tellus B, 52, 636–651,

925   doi:10.1034/j.1600-0889.2000.00025.x, 2000.

926   Wu, G. X., Li, Z. Q., Fu, C. B., Zhang, X. Y., Zhang, R. Y., Zhang, R. H., Zhou, T. J., Li, J. P., Li, J.

927   D., Zhou, D. G., Wu, L., Zhou, L. T., He, B., and Huang, R. H.: Advances in studying

928   interactions between aerosols and monsoon in China, Sci. China Earth Sci., 59: 1,

929   doi:10.1007/s11430-015-5198-z, 2016.

930   Xia, X., Zong, X., Cong, Z., Chen, H., Kang, S., and Wang, P.: Baseline continental aerosol over

931   the central Tibetan plateau and a case study of aerosol transport from South Asia, Atmos.

932   Environ., 45, 7370–7378, doi:10.1016/j.atmosenv.2011.07.067, 2011.

933   Xu, J., Bergin, M. H., Yu, X., Liu, G., Zhao, J., Marrico, C. M., and Baumann, K.: Measurement of

934   aerosol chemical, physical, and radiative properties in the Yangtze delta region of China, Atmos.

935   Environ., 36, 161–173, doi:10.1016/S1352-2310(01)00455-1, 2002.

936   Xu, J., Bergin, M. H., Greenwald, R., Schauer, J. J., Shafer, M. M., Jaffrezo, J. L., and Aymoz, G.:

937   Aerosol chemical, physical, and radiative characteristics near a desert source region of

938   northwest China during ACE–Asia, J. Geophys. Res., 109, D19S03,

939   doi:10.1029/2003JD004239, 2004.

940   Yan, H.: Aerosol scattering properties in northern China, Atmos. Environ., 41, 6916–6922,

941   doi:10.1016/j.atmosenv.2007.04.052, 2007.

942   Yan, P., Tang, J., Huang, J., Mao, J. T., Zhou, X. J., Liu, Q., Wang, Z. F., and Zhou, H. G.: The

943   measurement of aerosol optical properties at a rural site in Northern China, Atmos. Chem. Phys.,

944   8, 2229-2242, doi:10.5194/acp-8-2229-2008, 2008.

945   Yin, Y. and Chen, L.: The effects of heating by transported dust layers on cloud and precipitation:

946   a numerical study, Atmos. Chem. Phys., 7, 3497-3505, doi:10.5194/acp-7-3497-2007, 2007.

947   Zhang, X., Arimoto, R., and An, Z.: Dust emission from Chinese desert sources linked to

948   variations in atmospheric circulation, J. Geophys. Res., 102, D23, 28041–28047,

949   doi:10.1029/97JD02300, 1997.

950   Zhao, T. L., Gong, S. L., Zhang, X. Y., Blanchet, J. –P., McKendry, I. G., and Zhou, Z. J.: A

951   simulated climatology of Asian Dust aerosol and its Trans–Pacific transport. Part I: Mean

952   climate and validation, J. Climate, 19, 88–103, doi: 10.1175/JCLI3605.1, 2006.

953

954 **Figure captions**

955

956

957 **Table 1.** The main aerosol observing and other ground-based instruments deployed at Dunhuang
958 farmland during spring of 2012.

Measured variables	Model, Manufacturer	Accuracy
PM_{10} concentration	Ambient particulate monitor (RP1400a), R&P Corp.	0.1 μgm^{-3}
Aerosol scattering coefficient	Integrating nephelometer (TSI 3563), TSI Inc. 450, 550, and 700 nm	0.44, 0.17, and 0.26 Mm^{-1}
Aerosol absorption coefficient	Multi-angle absorption photometer (MAAP 5012), Thermo	0.66 Mm^{-1}
Aerosol size distribution	Aerodynamic particle sizer (APS 3321), TSI Inc., 0.5~20 μm	0.001 cm^{-3}
Aerosol-attenuated backscatter profile	Micro-pulse lidar (MPL–4), Sigma Space Corp.	Spatial resolution: ~30 m
Meteorological elements	Weather transmitter (WXT–520), Vaisala, Ta, RH, P, u, WD	Ta: ±0.3℃, RH: 0.1%, P: 0.1 hPa, u: 0.1 ms^{-1}, WD:1°
Global and diffuse radiation	Pyranometer (PSP[a,b]), Eppley Lab., 0.285～2.8 μm	Global: 8.46, diffuse: 8.48 $\mu VW^{-1}m^{-2}$
Direct radiation	Pyrheliometer (NIP[b]), Eppley Lab., 0.285～2.8 μm	8.38 $\mu VW^{-1}m^{-2}$
Downward long wave radiation	Pyrgeometer (PIR[a,b]), Eppley Lab., 3.5～50 μm	2.98 $\mu VW^{-1}m^{-2}$
24–bit color JPEG image	Total Sky Imager (TSI880), YES Inc., 352×288 pixel	Sampling rate: 1 minute

959 [a]The instrument is equipped with the Eppley ventilation system (VEN).
960 [b]The instrument is mounted on a two-axis automatic sun tracker (Model 2AP, Kipp&Zonen).

961

962

963 **Table 2.** Statistical summary of hourly average aerosol optical properties measured during
964 intensive observation period[a]

Variable	Mean	Std[b]	Median	10th percentile	25th percentile	75th percentile	90th percentile
PM_{10} (μgm^{-3})	113	169	54	17	29	111	300
σ_{sp} (Mm^{-1})	53.3	74.8	28.3	11.2	16.0	55.8	123.5
σ_{ap} (Mm^{-1})	3.20	2.40	2.50	1.27	1.69	3.90	5.94
SSA (670 nm)	0.913	0.055	0.923	0.850	0.892	0.949	0.967
SAE (450/700 nm)	0.45	0.45	0.42	–0.1	0.1	0.73	0.99

965 [a]All aerosol data reported for volumes under 1013.25 hPa and 20 ℃.
966 [b]Std denotes the standard deviation.

967

968

969

970

971

972

973

974
975
976
977
978

979
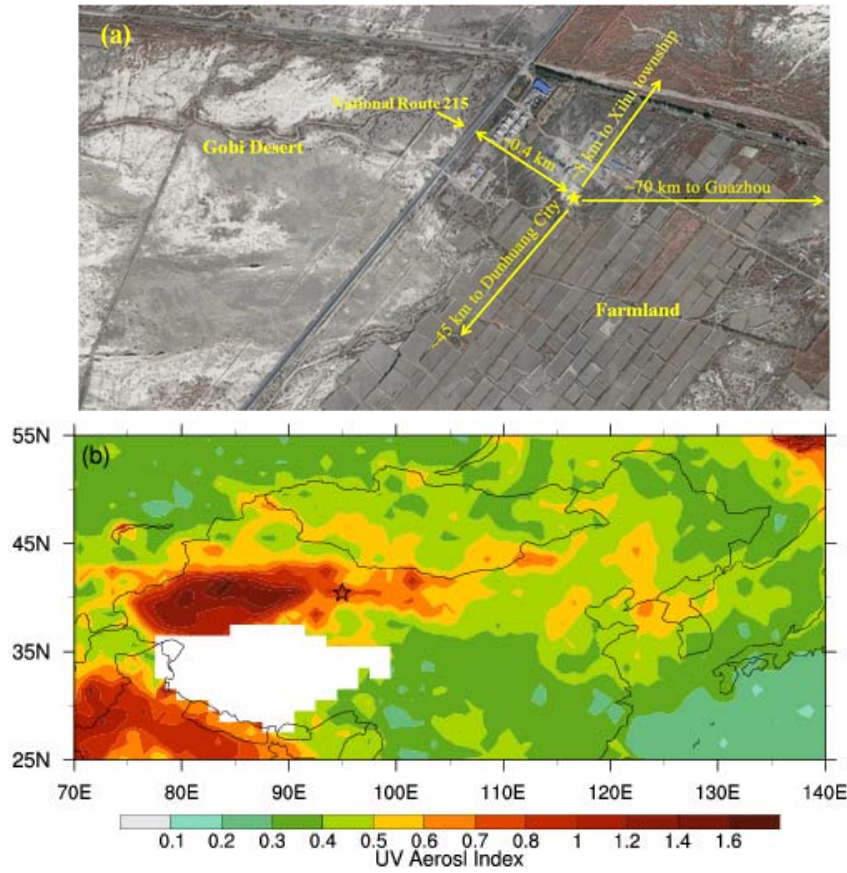
980
Figure 1. (a) The Dunhuang farmland site (40.492°N, 94.955°E, altitude: 1061 m) labeled with a
pentagram and its surrounding region. (b) OMI (Ozone Monitoring Instrument, 2004) mean UV
aerosol index from 1 April to 12 June 2012. The site is located in the downwind region of the
Taklimakan Desert and frequently outbreaks dust storms.

985
986
987
988
989
990
991
992
993
994
995
996
997
998
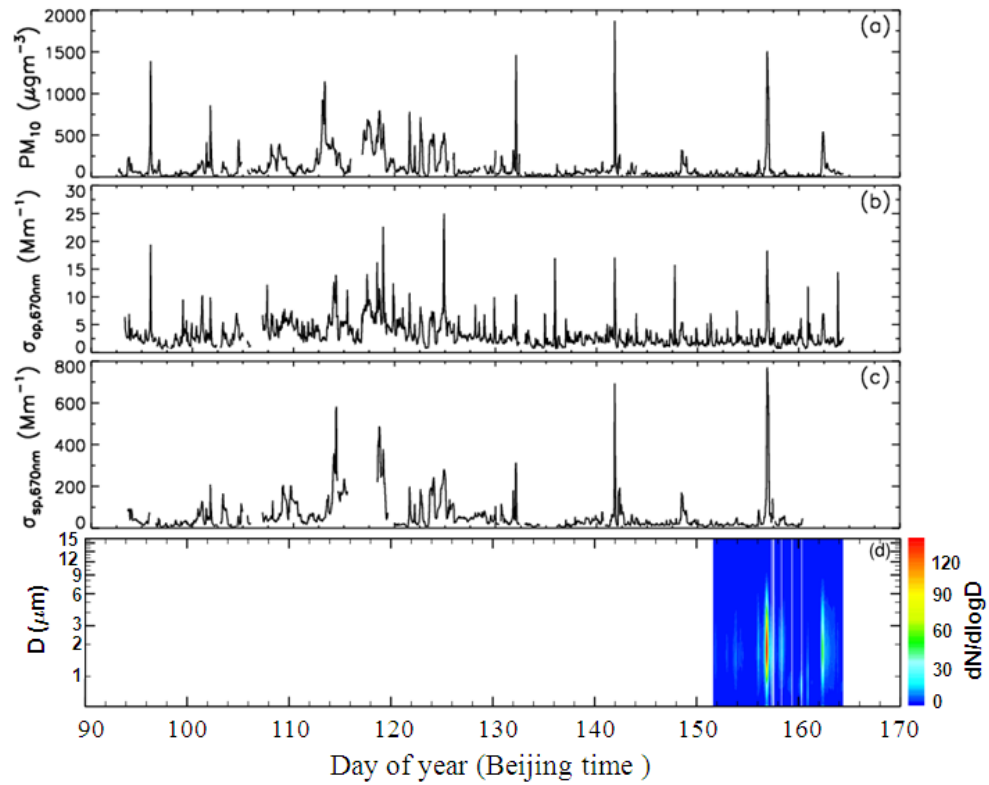
Figure 2. Time series of hourly average (a) PM_{10} mass concentration in μgm^{-3}, (b) aerosol absorption coefficient at 670 nm, (c) aerosol scattering coefficient at 670 nm, and (d) aerosol size distribution in cm^{-3} at Dunhuang farmland during the whole sampling period.
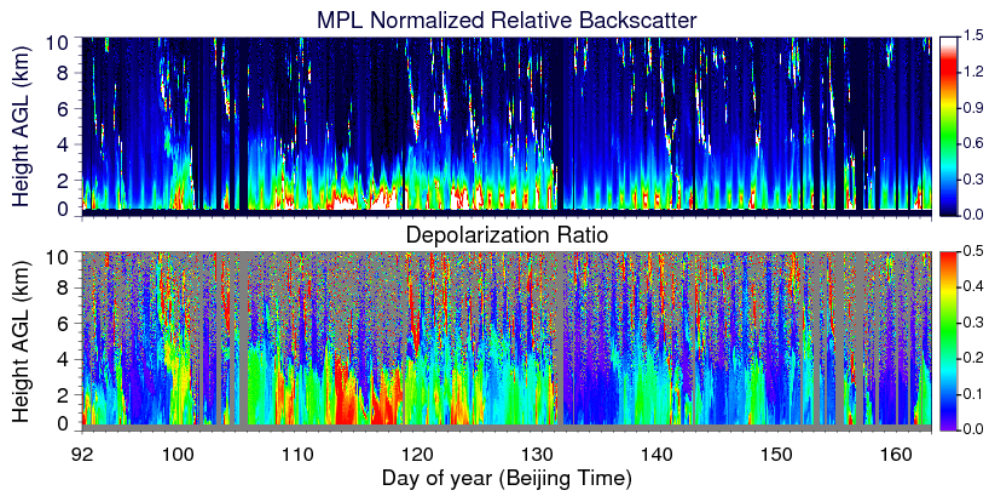
Figure 3. Time evolutions of the MPL normalized relative backscatter intensity (top panel) and depolarization ratio (bottom panel) at Dunhuang farmland from 1 April to 12 June 2012.

1014

1015

1016

1017

1018 **Figure 4.** The diurnal variations of (first row, left to right) wind vector (ms^{-1}), air temperature (T
1019 in ℃), relative humidity (RH in %), (second row, left to right) PM$_{10}$ concentration (μgm^{-3}),
1020 aerosol scattering coefficient at 670 nm ($\sigma_{sp,670}$ in Mm^{-1}), aerosol absorption coefficient at 670 nm
1021 ($\sigma_{ap,670}$ in Mm^{-1}), (third row, left to right) scattering Ångström exponent at 450–700 nm (SAE
1022 450/700 nm), aerosol single-scattering albedo at 670 nm (SSA$_{670}$), and aerosol size distribution
1023 (dN/dlogD in cm^{-3}) in Dunhuang site from 1 April to 12 June 2012 (30 May to 12 June for aerosol
1024 size distribution). Median values (red square) are shown to give a more apparent diurnal feature
1025 than mean values, which could be affected by several strong dust episodes. The 25th (blue
1026 diamond) and 75th (green triangle) percentiles for each hour of the day are also displayed.

1027

1028

1029

1030

1031

1032

1033

1034

1035

1036

1037

1038

1039

1040
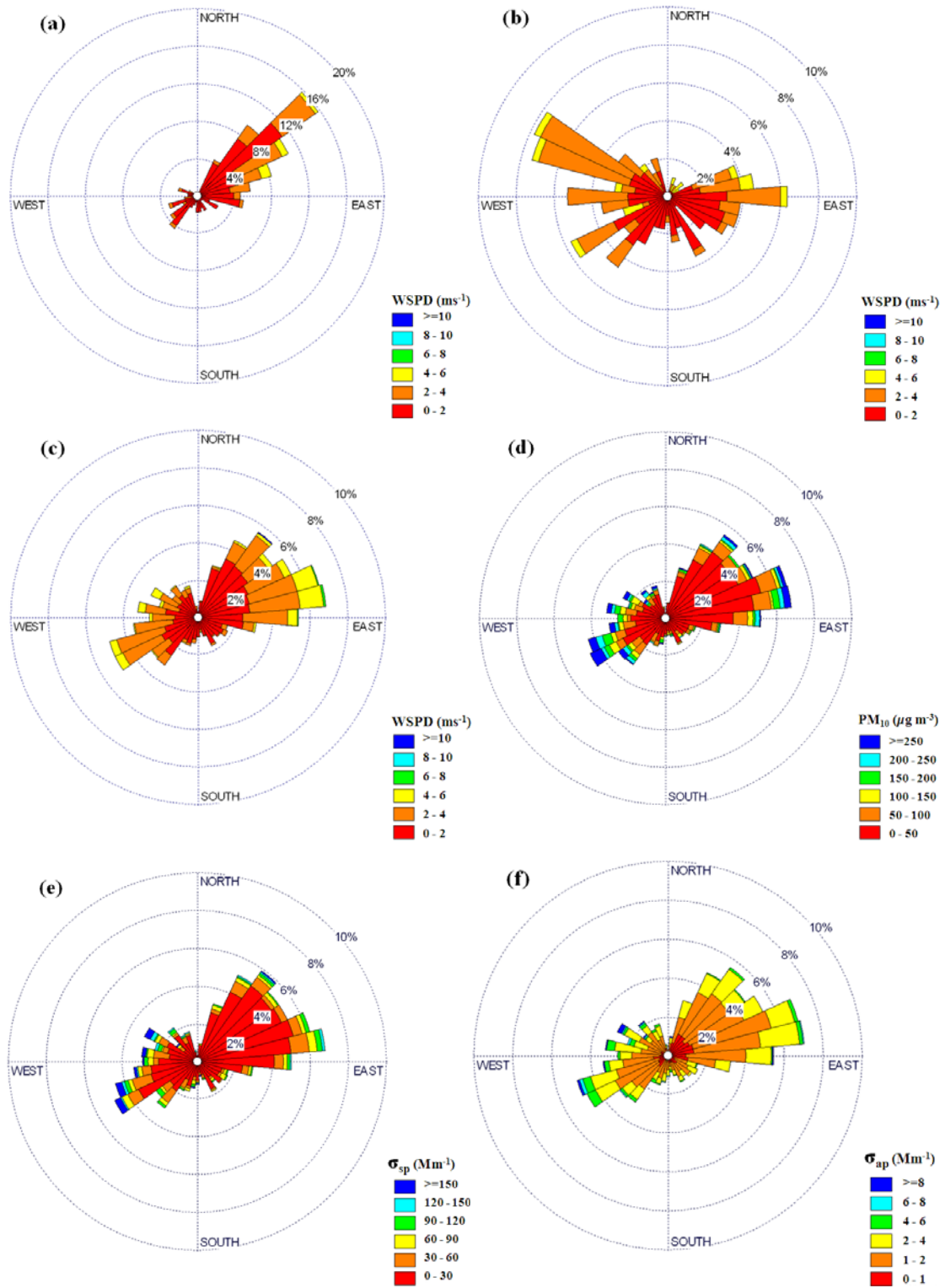
1041

1042

1043

Figure 5. Wind rose plots for (a) morning hour (06:00–09:00 LT), (b) evening hour (19:00–22:00 LT), and (c) all hours; shade represents wind speed (ms^{-1}). Wind roses for all hours, with shade representing levels of (d) PM$_{10}$ concentration (μgm^{-3}), (e) aerosol scattering coefficient at 670 nm (σ_{sp} in Mm^{-1}), and (f) aerosol absorption coefficient at 670 nm (σ_{ap} in Mm^{-1}).

1048
1049
1050
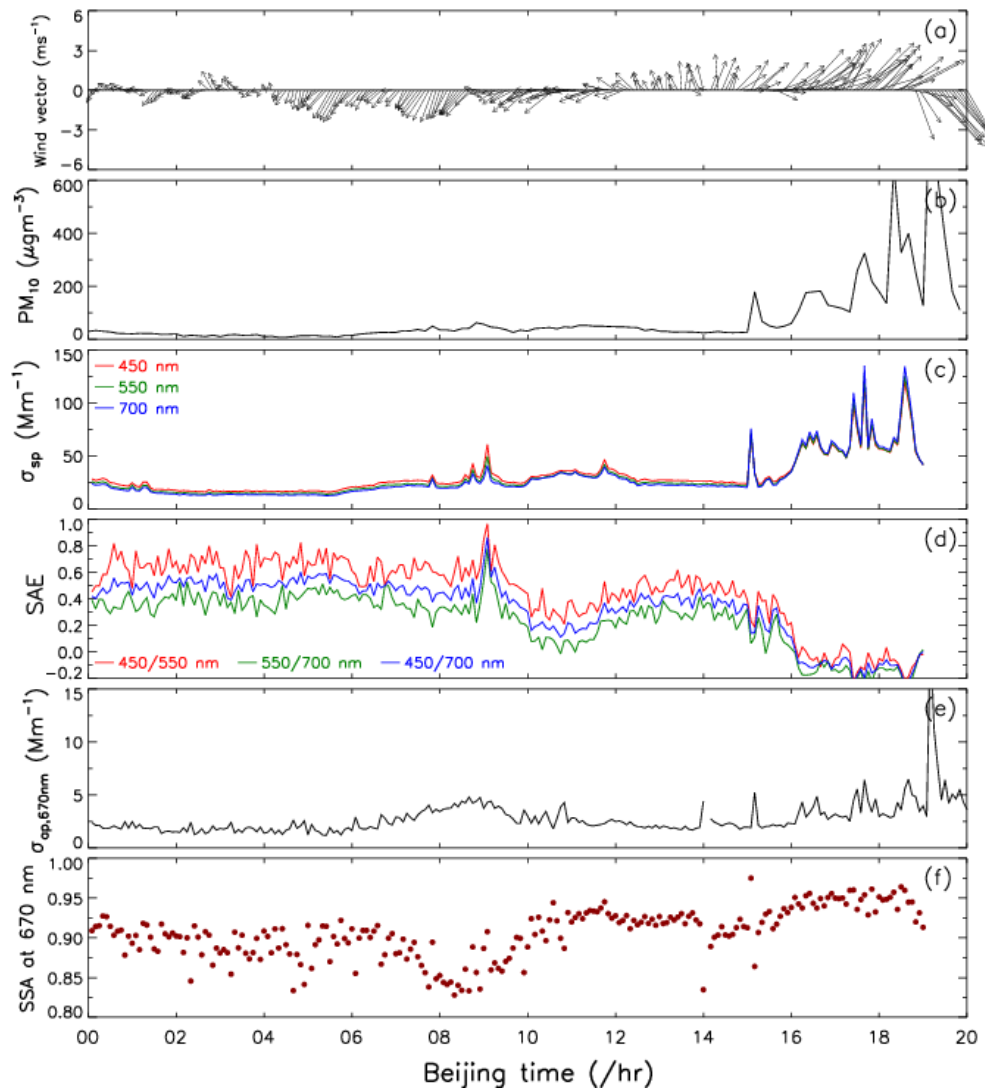
Figure 6. Time series of (a) wind vector (ms^{-1}), (b) PM$_{10}$ concentration (µgm^{-3}), (c) aerosol scattering coefficient (σ_{sp} in Mm^{-1}) at 450 nm (red), 550 nm (green), and 700 nm (blue), (d) scattering Ångström exponent (SAE) at 450–550 nm (red), 550–700 nm (green), and 450–700 nm (blue), (e) aerosol absorption coefficient at 670 nm (σ_{ap} in Mm^{-1}), and (f) single-albedo albedo at 670 nm (SSA$_{670}$) during a typical Tomb-sweeping Day on 4 April 2012, which implies a potential anthropogenic influence on aerosol optical properties. All data points are obtained from 5-minute average values.

1070

1071

1072

1073

1074

1075

1076

Figure 7. The wind fields (black arrows) at 500 hPa (left panel) and 850 hPa (right panel) levels during three heavy dust events on 30 April (top), 1 May (middle), and 10 June (bottom) 2012, based on MERRA reanalysis data. Note that the Dunhuang farmland is marked with a red pentagram and the white regions at 850 hPa are on behalf of the missing values.
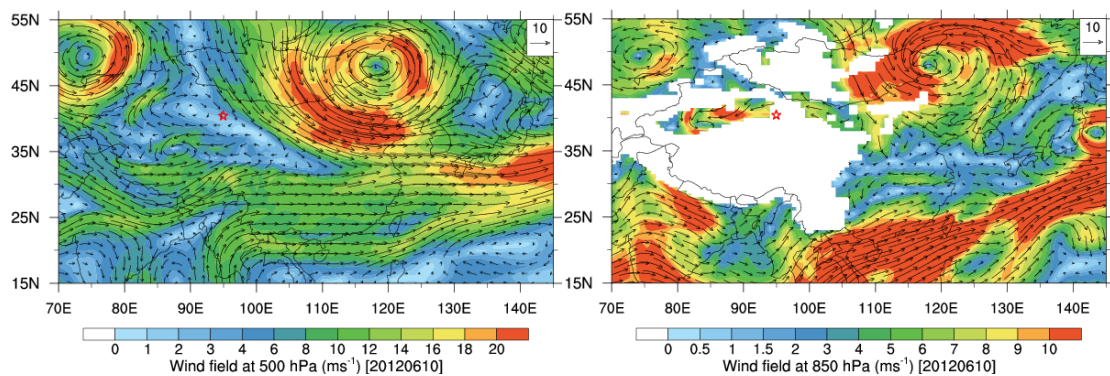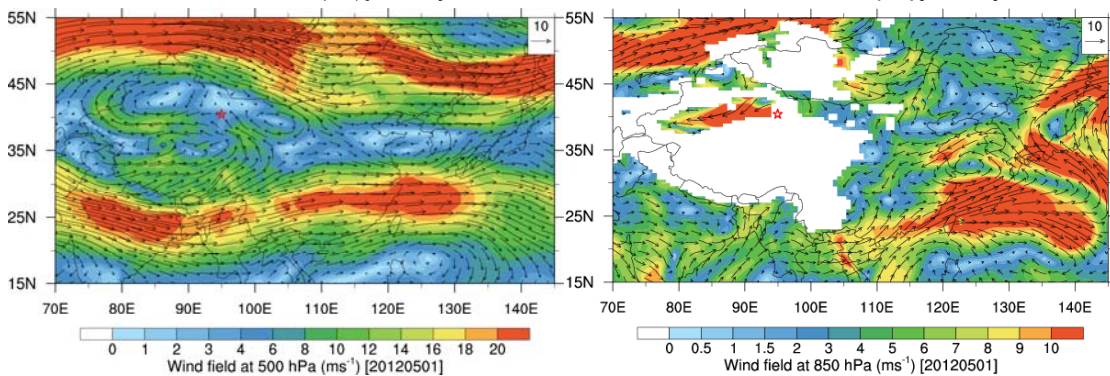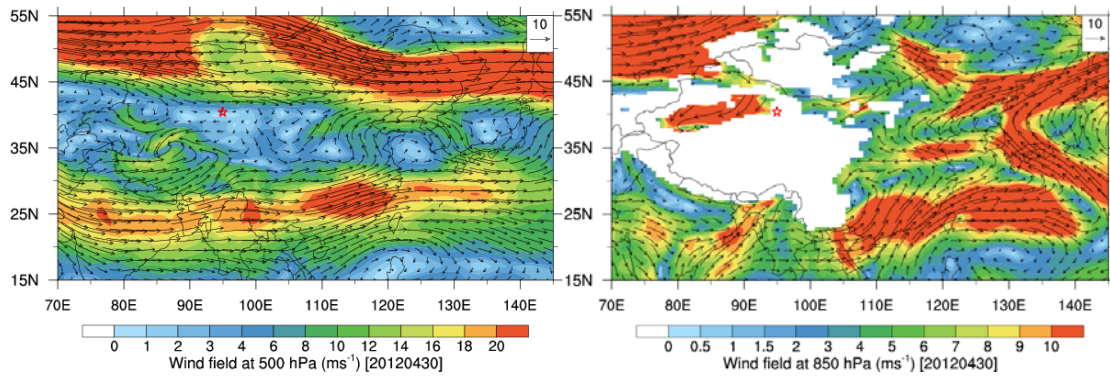
1081

1082

1083

1084

1085

1086

1087

1088

1089

1090

1091

1092

1093

1094

Figure 8. The same as Figure 6, except for (a) wind speed (ms^{-1}) and wind direction (^{o}) during three heavy dust events on 30 April, 1 May, and 10 June 2012. There were no measurements of aerosol scattering coefficient (σ_{sp} in Mm^{-1}) on 10 June due to equipment failure.
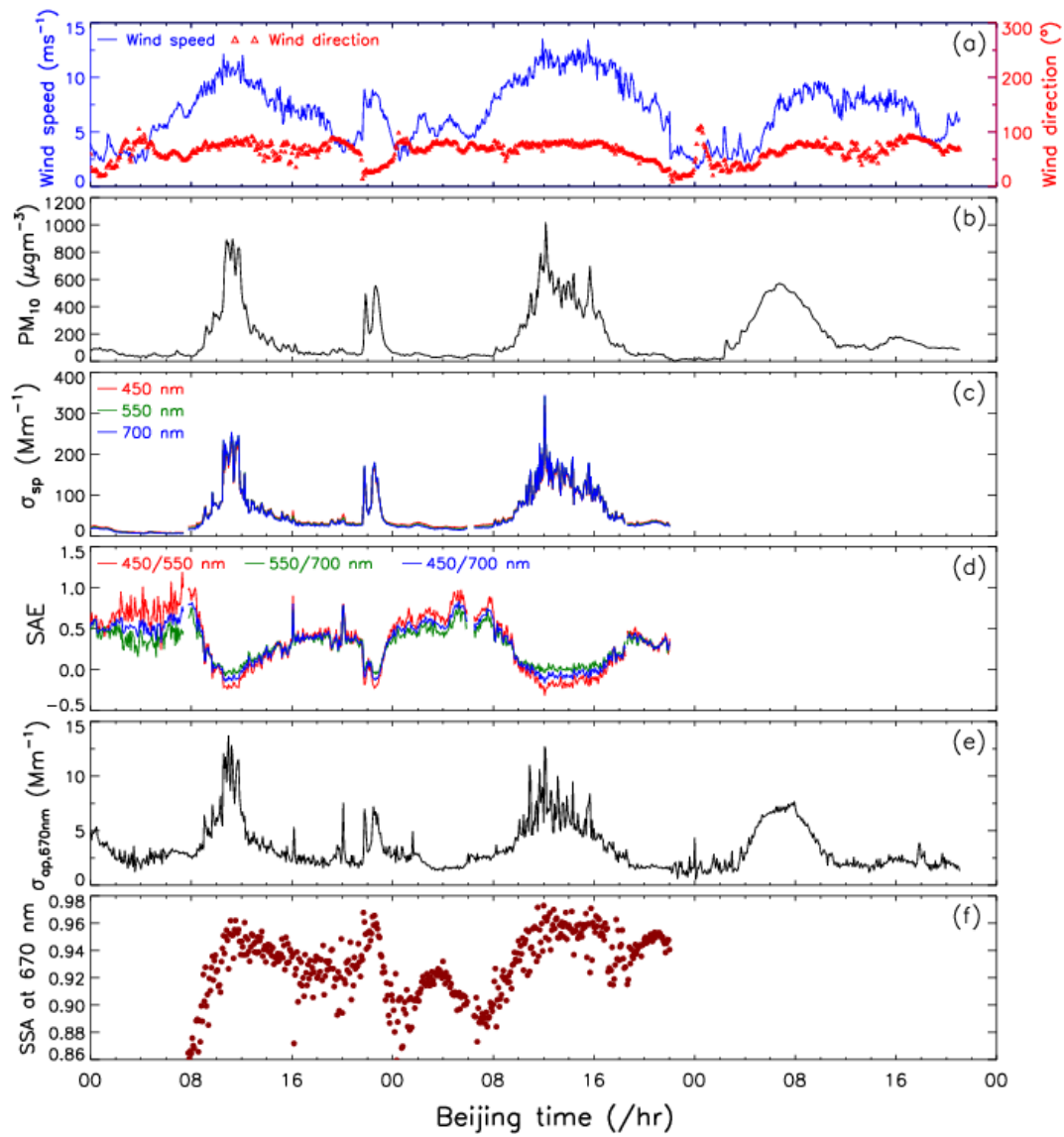
1098

1099

1100

1101

1102

1103

1104

1105
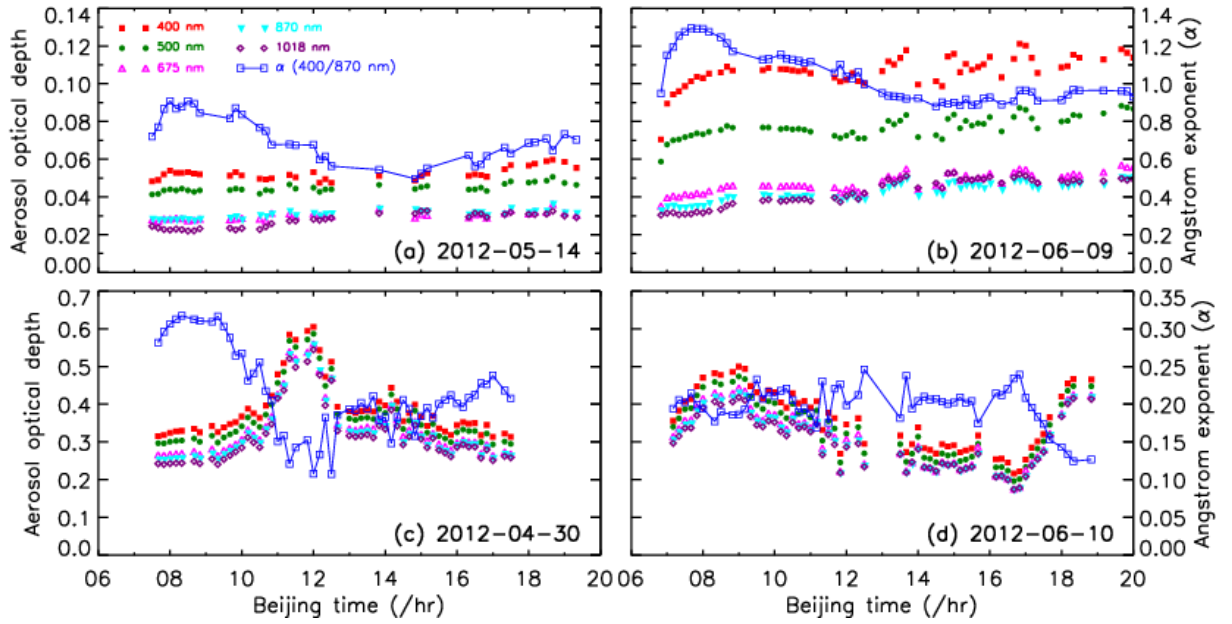
1106

1107 **Figure 9.** Time evolutions of aerosol optical depth (AOD) at five wavelengths (400, 500, 675, 870,

1108 and 1018 nm) versus Ångström exponent (α) at 400–870 nm on (a) 14 May, (b) 9 June, (c) 30

1109 April, and (d) 10 June 2012. Note that Figures 9(a)–9(b) are adopted from *Bi et al.* (2014) with an

1110 addition of the Ångström exponent plot in the original publication.

1111

1112
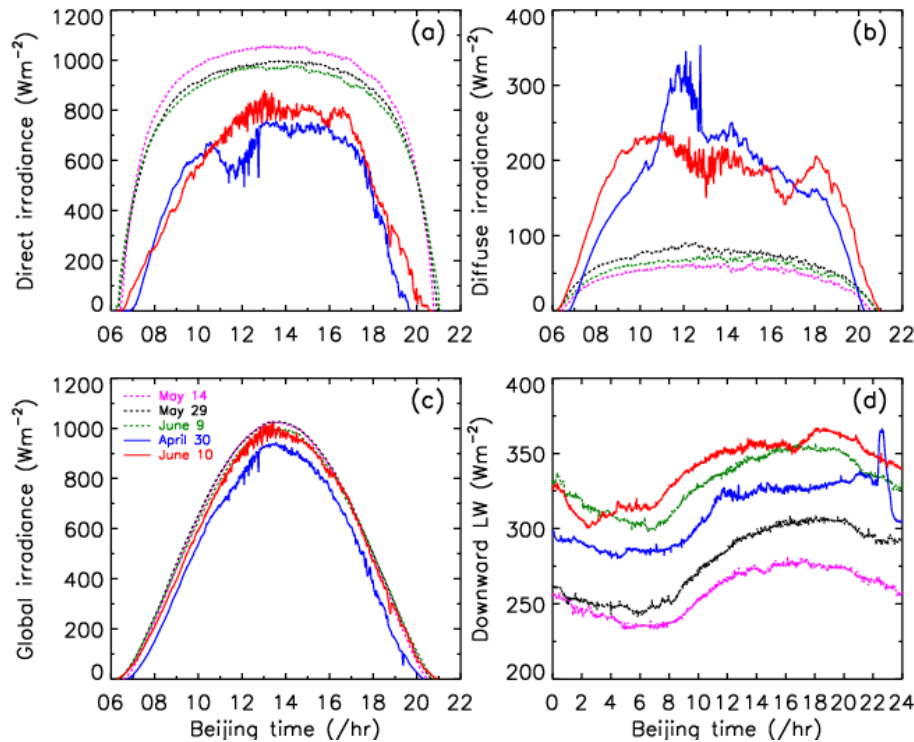
1113

1114 **Figure 10.** Diurnal variations of ground-based measurements of 1-minute average (a) direct, (b)

1115 diffuse, and (c) global irradiances, and (d) downward long wave irradiance under completely

1116 clear–sky conditions (14 May, 29 May, and 9 June) and dust events (30 April and 10 June).